This is a preprint, the final version is subject to change, of the American Mineralogist (MSA)
Cite as Authors (Year) Title. American Mineralogist, in press.
(DOI will not work until issue is live.) DOI: http://dx.doi.org/10.2138/am-2017-5878

Revision 1

Hydrogen incorporation mechanisms in forsterite: New insights from ^{1}H and ^{29}Si NMR spectroscopy and first-principles calculation

Xianyu Xue[1*], Masami Kanzaki[1], Doreen Turner[2] and Dominik Loroch[3]

[1]Institute for Planetary Materials, Okayama University, Misasa, Tottori 682-0193 Japan

[2]Institute of Geoscience, University of Jena, Burgweg 11, Jena 07749 Germany

[3]Institute for Mineralogy, University of Muenster, Corrensstrasse 24, Muenster, 48149 Germany

*Corresponding author; E-mail: xianyu@misasa.okayama-u.ac.jp

Tel: 81-858-43-3824

Submitted to Am. Mineral. June 9, 2016

Revised September 4, 2016

Abstract

The presence of water (hydrogen) in nominally anhydrous mantle minerals may have profound effects on their physical properties (e.g., electrical conductivity, diffusivity, rheology), and these effects are expected to depend on how water is incorporated in the crystal structure. For olivine, the most abundant upper mantle mineral, despite extensive studies, mostly using vibrational spectroscopy, the interpretations are still not well constrained. To provide better understanding on this issue, we carried out a comprehensive ^{1}H and ^{29}Si NMR study on an Mg_2SiO_4 forsterite sample containing about 0.5 wt% H_2O synthesized at 12 GPa and 1200 °C, complemented by Raman measurement and first-principles calculation of the geometry, stability and NMR parameters of model structures. The Raman spectra contain relative sharp O-H stretching bands near 3612, 3579 and 3567 cm^{-1} and a broader band near 3547 cm^{-1}, similar to previous reports. The ^{1}H static and MAS NMR data revealed that there are two main populations of protons in the hydrous forsterite structure, one experiencing strong ^{1}H-^{1}H homonuclear dipolar couplings and contributing to a broad

peak near 2.4 ppm, and another with weaker dipolar couplings and contributing to a narrower peak near 1.2 ppm in the MAS NMR spectrum at 30 kHz. Two-dimensional ^{1}H CRAMPS-MAS NMR measurements confirmed that the two proton components belong to the same phase and the contrast in MAS NMR peak width is largely due to difference in the strength of ^{1}H-^{1}H homonuclear dipolar couplings. In addition, there is also a very weak, narrow ^{1}H MAS NMR peak near 7.3 ppm (contributing to < 0.1% of the total intensity) due to protons that are more remote from the two main components. First-principles calculation confirmed that the two main proton components can be attributed to the hydrogarnet-like substitution mechanism of four H ions for one Si ($(4H)_{Si}$) in a tetrahedral site of olivine, but unlike hydrogarnet with one of the protons pointing away from the tetrahedral center and located in an adjacent interstitial site, thus experiencing weaker dipolar couplings than those in the vicinity of the vacant tetrahedron; the very weak narrow peak near 7.3 ppm can be attributed to the substitution mechanism of two H ions for one Mg in an M1 site ($(2H)_{M1}$) of forsterite. The ^{1}H-^{29}Si CP-MAS NMR spectra revealed both a broad peak encompassing the position for OH defect-free forsterite (-61.7 ppm) and a narrower peak at higher frequency (-60.9 ppm). First-principles calculation indicates that these peaks are accountable by the same models as for the ^{1}H NMR data. Thus, this study has provided unambiguous evidence supporting that hydrogen is incorporated in forsterite at relatively high pressure dominantly as $(4H)_{Si}$ defects, with $(2H)_{M1}$ defects playing only a very minor role. The much larger ^{1}H chemical shift for protons associated with the latter (than the former) is correlated with stronger hydrogen bonding for the latter, which in turn reflects difference in bonding environments of the OH groups (with the latter bonded to a Si, and the former only bonded to Mg). Similar correlation applies to the O-H stretching frequency. The $(4H)_{Si}$ defects are responsible for the observed high-frequency O-H stretching bands (> 3450 cm^{-1}), and the $(2H)_{M1}$ defects give lower frequencies (undetected here due to low abundance, but most likely near 3160-3220 cm^{-1} as previously reported) in vibrational spectra. These results can serve as a guide for (re-)interpretation of infrared and Raman spectroscopic data on hydrous olivine produced under different pressure and silica activity conditions, and require reconsideration of any models for the effects of water on physical properties of olivine based on different interpretations of such data. This study also demonstrated the usefulness of the combined solid-state NMR and first-principles calculation approach in unraveling

the hydrogen incorporation mechanisms in nominally anhydrous minerals.

Keywords: forsterite, water, structure, Si vacancy, Mg vacancy, NMR, first-principles calculation

Introduction

Water may be incorporated in many nominally anhydrous minerals as OH defects. The presence of even a small amount of water in minerals may strongly affect the phase relations, melting temperature and various physical properties (e.g., thermal and electrical conductivities, diffusivity, elastic property). Therefore, a large number of studies have been carried out so far in an attempt to understand the structure and physical properties of nominally anhydrous minerals (e.g., Keppler and Smyth 2006). To fundamentally understand the effect of water on the physical properties of minerals, knowledge of how water is incorporated in the crystal structure is indispensible, because different incorporation mechanisms can potentially have different effects on various properties.

Olivine, in particular, has been the focus of a large number of studies, because it is the most abundant constituent mineral of the upper mantle. The structure of olivine (*Pbnm* space group) consists of isolated SiO_4 tetrahedra that are interlinked by two types of MO_6 octahedra (M1 and M2 sites, occupied by Mg^{2+}, Fe^{2+}, etc.). It is known to accommodate significant amount of water (up to about 1 wt%) in the form of OH defects under upper mantle pressure and temperature conditions (Mosenfelder et al. 2006; Smyth et al. 2006). Most of the studies of hydrogen incorporation mechanisms in olivine have used vibrational spectroscopy, mostly infrared (e.g., Bai and Kohlstedt 1992; Bai and Kohlstedt 1993; Bali et al. 2008; Berry et al. 2005; Berry et al. 2007; Ferot and Bolfan-Casanova 2012; Gaetani et al. 2014; Ingrin et al. 2013; Koch-Muller et al. 2006; Kohlstedt et al. 1996; Kovacs et al. 2010; Kovacs et al. 2012; Kudoh et al. 2006; Lemaire et al. 2004; Libowitzky and Beran 1995; Matsyuk and Langer 2004; Matveev et al. 2001; Miller et al. 1987; Mosenfelder et al. 2006; Smyth et al. 2006; Walker et al. 2007; Withers et al. 2011; Yang 2016), but also some Raman (Bolfan-Casanova et al. 2014; Hushur et al. 2009; Manghnani et al. 2013). A few studies also used single-crystal X-ray diffraction (Hushur et al. 2009; Kudoh et al. 2006; Smyth et al. 2006). Vibrational

spectroscopic measurements on synthetic and natural olivine samples have revealed a large number of bands due to O-H stretching vibrations in the 3000-3700 cm^{-1} region; the number, frequencies and intensities of O-H stretching bands have been reported to vary depending on factors such as the composition (silica activity, Fe/Mg ratio, presence/absence of impurity cations such as Ti^{4+}, Cr^{3+}, Al^{3+}), oxygen fugacity, and pressure and temperature conditions. To better constrain the spectral assignment, some of these studies have focused on hydrogen incorporation in the chemically simpler Mg_2SiO_4 forsterite. The reported infrared and Raman spectra for forsterite (and often $(Mg,Fe)_2SiO_4$ olivine as well) synthesized at relatively high pressures (> 3 GPa) are generally dominated by several bands in the high-frequency (3450-3650 cm^{-1}) region, regardless of silica activity (e.g., Bali et al. 2008; Kohlstedt et al. 1996; Mosenfelder et al. 2006; Otsuka and Karato 2011; Smyth et al. 2006; Withers et al. 2011). Infrared spectra for forsterite (and often also $(Mg,Fe)_2SiO_4$ olivine) samples synthesized at lower pressures (< 3 GPa) seem to show more prominent dependency on silica activity: samples produced at low silica activities (bulk M/Si ratio ≥2) mostly show infrared bands dominantly in the high-frequency region (> 3450 cm^{-1}) similar to those produced at higher pressures, whereas samples produced under high silica activities (bulk M/Si ratio <2) have been reported to exhibit bands at lower frequencies (near 3160 or 3220 cm^{-1}), either dominantly or coexisting with higher-frequency bands (e.g., Bali et al. 2008; Berry et al. 2005; Demouchy and Mackwell 2003; Grant et al. 2006; Lemaire et al. 2004; Padrón-Navarta et al. 2014). Interpretations of these vibrational O-H stretching bands have been controversial for a long time. For example, the high-frequency O-H stretching bands (> 3450 cm^{-1}) have been interpreted in terms of substitution of two H ions for one Mg (e.g., Hushur et al. 2009; Kudoh et al. 2006; Manghnani et al. 2013; Otsuka and Karato 2011; Smyth et al. 2006), or four H ions for one Si (hydrogarnet-like) (e.g., Berry et al. 2005; Kovacs et al. 2010; Matveev et al. 2001), or both (e.g., Lemaire et al. 2004). Interstitial OH groups were also postulated in earlier studies (Bai and Kohlstedt 1992; Bai and Kohlstedt 1993; Kohlstedt et al. 1996). The assignment of the high-frequency bands to H ions associated with Mg vacancies (or interstitial OH groups) was mostly based on indirect evidence, such as cation site occupancies and (average) O-O edge lengths determined from structural refinement of X-ray diffraction data (Hushur et al. 2009; Kudoh et al. 2006; Manghnani et al. 2013; Smyth et al. 2006) or thermodynamic argument based on the

observed water solubility as a function of water fugacity (Bai and Kohlstedt 1992; Bai and Kohlstedt 1993; Kohlstedt et al. 1996; Otsuka and Karato 2011). As will be further discussed below, there are pitfalls in some of these arguments. For example, the O-O edge lengths tend to be locally relaxed around OH defects, and thus wrong conclusion may result if one assumes that the average O-O edge lengths obtained from diffraction methods for a nominally anhydrous mineral are correlated with the O-H stretching frequencies (Blanchard et al. 2009; Umemoto et al. 2011, also see discussions below). The observed change in infrared spectra with silica activity at <3 GPa, on the other hand, has been suggested to be consistent with the assignment of (most of) the high-frequency O-H stretching bands to H ions associated with Si vacancies (Berry et al. 2005; Lemaire et al. 2004; Matveev et al. 2001). More direct information about the nature of the individual vibrational bands came from theoretical calculations. A number of studies have used computational methods to evaluate the stability (Balan et al. 2011; Brodholt and Refson 2000; Haiber et al. 1997; Umemoto et al. 2011; Verma and Karki 2009; Walker et al. 2006; Walker et al. 2007; Wright and Catlow 1994) and infrared spectroscopic characteristics (Balan et al. 2014; Balan et al. 2011; Braithwaite et al. 2003; Crepisson et al. 2014; Shaw and Tse 2007; Umemoto et al. 2011; Walker et al. 2006) of different OH defects in forsterite. The more recent first-principles density-functional theory (DFT) calculations by Balan et al. (2011) and Umemoto et al. (2011), in particular, provided strong evidence supporting that H ions associated with Si vacancies give high-frequency O-H stretching bands (> 3450 cm^{-1}), and those associated with Mg vacancies give low-frequency bands (most likely corresponding to the observed bands near 3160-3220 cm^{-1}). Nevertheless, detailed assignments of the individual observed vibrational bands in the high-frequency region, including the nature for some of them, are still not well constrained, and the interpretation apparently has not been universally accepted. For example, there was postulation for the assignment of one or two high-frequency O-H stretching bands that exhibit stronger temperature-dependent broadening and frequency shift (including a commonly observed, major band near 3550 cm^{-1} at room temperature) to (charged) interstitial OH groups from low-temperature infrared measurement (Ingrin et al. 2013) and first-principles calculation (Balan et al. 2014). As will be discussed below, this is questionable considering that the presence of charged defects of major abundance is energetically unfavorable. Even more recently, authors of some publications

(e.g. Karato 2013; Karato 2015; Manghnani et al. 2013) still regard hydrogen to be primarily associated with Mg vacancies, when the vibrational spectra of the corresponding olivine samples consist dominantly of high-frequency O-H stretching bands. Therefore, there is a need to better clarify the nature of hydrogen incorporation in olivine, by obtaining additional constraints from complementary spectroscopic techniques, such as nuclear magnetic resonance (NMR) spectroscopy.

Solid-state NMR may potentially place better constraints on the incorporation mechanisms of water (and other structural issues) in minerals, because it can provide detailed and quantitative local structural information around individual elements (nuclei, e.g., ^{29}Si, ^{1}H) and their spatial relationship, via a rich variety of multi-nuclear, multi-resonance and multi-dimensional NMR techniques (Xue and Kanzaki, 2009; Stebbins and Xue, 2014). This is particularly true when the full capacity of advanced NMR techniques is combined with first-principles calculation (Griffin and Ashbrook 2013; Griffin et al. 2013; Xue and Kanzaki 2009). Kohn (1996) first applied ^{1}H magic-angle spinning (MAS) NMR to a forsterite sample (and some other nominally anhydrous minerals) synthesized at 1.5 GPa and 1000-1150 °C under water-saturated condition, and identified several narrower peaks (including an intense peak near 1 ppm and smaller features near 6.9 ppm and possibly also 5.5 ppm) on top of a broad peak (near 4.3 ppm). Unfortunately, because of the presence of excess water in the sample and complication with sample handling (crushed in water before NMR measurement), it was not certain whether a significant part of the observed intensities could be due to coexisting quenched hydrous phases and/or water in grain boundaries (e.g., Keppler and Rauch 2000). A subsequent study on another forsterite sample synthesized at 2.1 GPa and 1100 °C described in Kohn (2006) reported an "improved" ^{1}H MAS NMR spectrum that contains a broad peak at 1 ppm (in addition to a background signal) and a distinct peak at 6.7 ppm, without the dominant broader feature in the earlier spectrum. However, there was still some ambiguity regarding the extent of contribution from coexisting quenched hydrous phases and water in grain boundaries to the observed spectrum. Note that these studies did not utilize the diverse NMR techniques available to strengthen peak assignment.

In this study, we performed detailed one-dimensional ^{1}H static and MAS NMR, ^{29}Si MAS NMR and ^{1}H-^{29}Si

cross-polarization (CP) MAS NMR measurements, and two- dimensional (2D) ^{1}H homonuclear correlation MAS NMR experiments, in addition to Raman measurement, on a nearly single-phase forsterite sample containing about 0.5 wt% H_2O (water-undersaturated) synthesized at 12 GPa and 1200 °C, and also carried out first-principles calculation to help interpret the experimental data. It will be shown that these data provided unambiguous evidence for the hydrogen incorporation mechanisms in forsterite, and revealed that the dominant incorporation mechanism is four H ions substituting for one Si (denoted $(4H)_{Si}$ hereafter), with trace amount of protons incorporated via the substitution mechanism of two H ions for one Mg in an M1 site (denoted $(2H)_{M1}$ hereafter). The former corresponds to relatively high-frequency O-H stretching frequencies (> 3450 cm^{-1}) and the latter to lower frequencies in vibrational spectra. These data thus supplied the long-needed guide for the interpretation of vibrational spectroscopic data for hydrous forsterite (and olivine in general).

Experimental and Calculation Methods

Sample synthesis and description

An anhydrous Mg_2SiO_4 forsterite sample was first synthesized by heat treatment of a mixture of reagent-grade MgO and SiO_2, initially at 1300 °C for 20 hr and then at 1500 °C for 24 hr, with thorough grinding/mixing and pelleting prior to each heating stage. The MgO and SiO_2 starting materials had been dried at 1000 °C and 1200 °C, respectively, for 12 hr before use.

A hydrous Mg_2SiO_4 forsterite sample containing nominally 0.5 wt% H_2O was synthesized at 12 GPa and 1200 °C for 1 hr in a 5000-ton Kawai-type double-stage uniaxial split-sphere multi-anvil press. Previous studies reported water solubility of 0.55-0.89 wt% in forsterite at about 12 GPa and 1100-1250 °C (Litasov et al. 2007; Smyth et al. 2006). The target water content of 0.5 wt% was chosen so that the sample is under-saturated with water to avoid possible coexisting quenched fluid phases. The starting material was Mg_2SiO_4 forsterite plus a $2Mg(OH)_2 + SiO_2$ mixture with the target bulk composition. The SiO_2 starting material is the same as described above, and the $Mg(OH)_2$ starting material is reagent-grade and had been dried and stored in an oven at 110 °C before use. The $2Mg(OH)_2 + SiO_2$

starting mixture was first prepared by thoroughly grinding and mixing the ingredients in an agate mortar and then drying in an oven at 110 °C for ca. 24 hr; this mixture was then weighed and mixed with Mg_2SiO_4 forsterite and thoroughly ground and mixed again, and finally dried in an oven at 110 °C for > 16 hr before sealed into a Pt capsule (2 mm outer diameter and ~3 mm length). For high-pressure sample synthesis, a Cr-doped MgO octahedral cell assembly of an edge length of 14 mm was used. The Pt capsule was put at the center of the octahedron, and was surrounded by an MgO tube, a tube heater made of hBN plus TiB_2 and a ZrO_2 sleeve, as described in Kanzaki (2010). The temperature was measured with a $W_{97}Re_3$-$W_{75}Re_{25}$ thermocouple with an uncertainty within ca 2 ° C. The pressure was estimated from a pressure calibration curve constructed from an in-situ X-ray diffraction study with the same pressure cell (Kanzaki 2010) with an uncertainty less than 1 GPa.

The sample was recovered from the capsule under ambient condition after carefully cleaning the exterior of the capsule. The recovered sample was un-sintered and white-colored. It was confirmed to be a nearly pure forsterite sample by micro-Raman, electron microprobe and ^{29}Si MAS NMR measurements, with minor coexisting clinoenstatite revealed by ^{29}Si MAS NMR (see below). Both micro-Raman and ^{1}H MAS NMR confirmed that the added water was incorporated in the forsterite structure, and the estimated bulk water content (0.45(1) wt%) from quantitative ^{1}H MAS NMR spectra is in reasonable agreement with the nominal water content (see below).

Electron Microprobe Analysis

A small portion of the sample was embedded in epoxy and polished for examination with a JEOL JXA-8530F field-emission electron microprobe (FE-EPMA) at IPM. Back-scattered electron image observation and elemental (Mg, Si) mapping analysis revealed that the sample consisted of fine-grained forsterite with crystallite sizes of a few micrometers. The grain sizes were too small to allow accurate quantitative chemical analysis. No phases other than forsterite were detected with EPMA examination.

Raman spectroscopy

Unpolarized Raman spectra within the 200-1600 cm^{-1} and 2600-3700 cm^{-1} regions were acquired on selected grains using an argon-ion laser with a wavelength of 488 nm and a power of 60 mW in a 180° backscattering geometry, similar to that described previously (Xue et al. 2010). The laser beam was focused onto the sample with a 50× objective lens. Scattered light from the sample was focused onto a pinhole (diameter: 200 μm) before entering an imaging monochromater with a focal length of 500 mm and a grating of 1200 gr/mm, and was detected with a liquid nitrogen-cooled CCD detector. Raman shift was calibrated using the plasma lines of the laser with an accuracy better than 1 cm^{-1}. The exposure time was typically 60 s. Only forsterite was detected by Raman spectroscopy.

NMR spectroscopy

The recovered sample was loaded into an NMR rotor as is (without grinding), with special care in sample/rotor handling (e.g., wearing gloves and carefully cleaning rotor parts and packing tools) to avoid contamination. ^{1}H and ^{29}Si NMR spectra were obtained at room temperature at a resonance frequency of 400.4 and 79.5 MHz, respectively, using a Varian 9.4 tesla Unity-Inova NMR spectrometer and a 1.6 mm T3 MAS NMR probe. The chemical shifts for both nuclei were referenced to tetramethylsilane (TMS), and were reproducible to better than about ± 0.1 ppm.

^{1}H static and MAS NMR spectra (at 10-30 kHz spinning rates) were obtained on the hydrous forsterite sample (~14 mg) with a spectral width of 1 MHz and several recycle delay times up to 60 s (> $5\times T_1(^{1}H)$, where T_1 is the spin-lattice relaxation time constant). The ^{1}H T_1 was measured with the saturation-recovery method, and was found to be 10.6(6) s for the main peaks (see below). The DEPTH sequence that consists of three back-to-back pulses ($\pi/2$-π-π) with a 16-step phase cycle (Cory and Ritchey, 1988) was used to suppress the probe background from outside the RF coil. The residual small background signal from the probe/rotor was subtracted from the reported spectra, by acquiring the corresponding spectra for the empty rotor. The bulk water content of the hydrous forsterite sample was estimated from the total intensities of the fully relaxed ^{1}H MAS NMR spectra (obtained with a recycle delay time of 60 s), using adamantane ($C_{10}H_{16}$) as an external intensity standard. Our previous study on hydrous aluminosilicate glasses (containing about 0.5-1 wt% H_2O) confirmed that water contents estimated in this way agree well (within about 0.1

wt%) with those determined by infrared spectroscopy (Malfait and Xue 2010).

Although NMR is a bulk technique, it is possible to utilize various two-dimensional (2D) single- and double-resonance techniques to gain information about the proximities of different atoms (within the same or different phases), which place further constraints on peak assignment. In this study, we applied two related 2D ^{1}H MAS NMR experiments. The first is 2D ^{1}H rotor-synchronized nuclear Overhauser effect spectroscopy (NOESY) experiment using the standard three-pulse ($\pi/2$ - t_1 - $\pi/2$ - t_{mix} - $\pi/2$ - acquire) sequence, similar to that described previously (Xue and Kanzaki 2007a; Xue et al. 2008). It probes the transfer of z magnetization between dipolar-coupled spins via spin diffusion during the mixing period (t_{mix}) (Brown 2007). Whereas protons that are isolated from one another (e.g., those belonging to different phases) yield only diagonal peaks (peaks with the same frequency in both dimensions), a pair of dissimilar protons that are dipolar-coupled (due to spatial proximity in the same phase) can produce both diagonal and cross peaks (peaks that are located at different frequencies in the two dimensions). The intensity ratio between the cross peak and diagonal peak increases with mixing time at a rate that depends on the ^{1}H-^{1}H distance, and ultimately levels off as spin diffusion approaches an equilibrium state. 2D rotor-synchronized ^{1}H NOESY MAS NMR spectra were acquired at a spinning rate of 20 kHz, a recycle delay time of 15 s (with one steady-state point acquired) and mixing times (t_{mix}) of 2 μs and 200 ms. Spectral widths in both dimensions were set to the rotor frequency. Sixteen transients were averaged for each of 64-160 t_1 increments. Even 160 t_1 increments were insufficient to allow complete decay of the signal for the narrowest peak observed (near 7.3 ppm), but this does not affect the overall conclusion.

As will be shown later on, some of the ^{1}H MAS NMR peaks are very broad. In order to ascertain whether the broad peak width is due to structure disorder or strong ^{1}H-^{1}H dipolar couplings (or both), we also performed 2D ^{1}H CRAMPS-MAS NMR experiment, similar to that described previously (Xue and Kanzaki 2007b; Xue et al. 2010). Like the NOESY experiment, the pulse sequence consists of three-pulses ($\pi/2$ - t_1 - $\pi/2$ - t_{mix} - $\pi/2$ - acquire), except that during the t_1 evolution period, frequency-switched Lee-Goldburg (FSLG) decoupling was applied to eliminate ^{1}H-^{1}H dipolar coupling (Bielecki et al. 1989; Vinogradov et al. 1999). The 2D CRAMPS-MAS NMR spectra were obtained on a smaller sample (6.5 mg) located at the central half portion (~4 mm length) of the rotor to improve RF field

241 homogeneity. A spinning rate of 25 kHz, a recycle delay time of 15 s, and mixing times (t_{mix}) of 2 μs and 200 ms were
242 used. Thirty-two scans were averaged for each t_1 time increment of 105 μs (corresponding to an un-scaled F_1 spectral
243 width of 9524 Hz). An RF field of ~110 kHz and an offset corresponding to the Lee-Goldburg (LG) condition were
244 applied during FSLG decoupling. The scaling factor for the CRAMPS dimension was found to be 0.58 from spectra
245 acquired with three different offsets (differing by 0 and ± 1 kHz). The corrected chemical shift scale for the CRAMPS
246 dimension is used for the reported spectra.

247 Single-pulse ^{29}Si MAS NMR spectra were obtained using a 1 μs-pulse (45° flip angle) and a recycle delay time of
248 2000 s at a spinning rate of 20 kHz, with 66 scans averaged. ^{1}H-^{29}Si CP-MAS NMR spectra were acquired at a
249 spinning rate of 20 kHz under the MAS-modified Hartman-Hahn condition (+1 spinning sideband for the ^{1}H channel),
250 with an RF field of ~50 kHz for the ^{29}Si channel and a ramped power (~8 kHz RF field range) for the ^{1}H channel. Spin
251 temperature inversion was incorporated in the phase cycle to eliminate direct polarization. A recycle delay of 15 s and
252 a range of contact times of 2-20 ms were used. 7260 to 17920 scans were averaged for the reported spectra.
253

254 **First-principles calculation**

255 First-principles density functional theory calculations of NMR parameters were performed for periodic structures
256 with the Gauge-Including Projector-Augmented Wave (GIPAW) method (Pickard and Mauri 2001) using the
257 Quantum-ESPRESSO (QE) package (version 5.3.0) (Giannozzi et al. 2009), similar to our recent study on
258 $(Mg,Zn)_2SiO_4$ olivine solid solution (Kanzaki and Xue 2016). A number of model structures of 2 × 1 × 2 supercell for
259 Mg_2SiO_4 forsterite (containing 16 formulae and 112 atoms, relative to the space group *Pbnm*) with one Si replaced by
260 four H atoms or one Mg in an M1 or M2 site replaced by two H atoms were studied. In order to provide chemical shift
261 reference and to double-check the reproducibility of experimental NMR data, similar calculations were also performed
262 on several other phases in the MgO-SiO_2-H_2O system, including H-free Mg_2SiO_4 forsterite and its two high-pressure
263 polymorphs (wadsleyite and ringwoodite), $MgSiO_3$ protoenstatite, orthoenstatite and low-pressure clinoenstatite,
264 phase A ($Mg_7Si_2O_8(OH)_6$), phase B ($Mg_{12}Si_4O_{19}(OH)_2$), superhydrous B ($Mg_{10}Si_3O_{14}(OH)_4$) and brucite ($Mg(OH)_2$).

The structures (both cell parameters and atomic coordinates) were first relaxed at 0 GPa with the PWscf code of the QE package, before NMR calculation using the GIPAW method implemented in the QE-GIPAW package (version 5.3.0). In addition to producing more reliable NMR parameters, the full relaxation of the structures (both cell parameters and atomic coordinates) makes it possible to directly compare with experimentally determined crystal structural parameters, which may provide additional constraints on the validity of different models. Both structural relaxation and NMR parameter calculations were performed using the PBEsol functional within the generalized gradient approximation (GGA) for the exchange-correlation energy (Perdew et al. 1996; Perdew et al. 2008). The PAW-pseudopotentials from the PSlibary ((Dal Corso 2014)) (Mg.pbesol-n-kjpaw_psl.0.3.0.UPF, Si.pbesol-n-kjpaw_psl.0.1.UPF, O.pbesol-n-kjpaw_psl.0.1.UPF, H.pbesol-kjpaw_psl.0.1.UPF) were adopted. A Monkhorst-Pack grid of 2 × 2 × 2 for the Brillouin zone sampling was used for the 2 × 1 × 2 supercell of forsterite, and comparable or finer grid sizes (with respect to the cell dimension, e.g., 4 × 2 × 4 grid for forsterite of a single unit cell) were used for the other phases. A kinetic energy cutoff of 50 Ry and a charge density cutoff of 250 Ry were used for all the reported data. To test whether these cutoff values are sufficient, additional test calculations on forsterite and phase A were also performed with a larger kinetic energy cutoff of 100 Ry and a charge density cutoff of 500 Ry during both structural relaxation and NMR calculations. The resultant total energy per atom and ^{29}Si and ^{1}H isotropic chemical shielding values differ from those calculated with a kinetic energy cutoff of 50 Ry and a charge density cutoff of 250 Ry by < 1 mRy and < 0.1 ppm, respectively; the corresponding relative differences between different structures are even smaller (by about one order). Therefore, the kinetic energy cutoff of 50 Ry and charge density cutoff of 250 Ry are considered sufficient.

The relaxed Mg_2SiO_4 forsterite structure at 0 GPa has the following cell parameters: a = 4.7613 A^3, b = 10.2037 A^3, c = 5.9867 A^3. The unit-cell volume is 290.85 A^3, only slightly larger (by 0.26%) than that determined by single-crystal X-ray diffraction under ambient condition (290.107(17) A^3, Smyth et al. (2006), also see Table 1). The calculated unit-cell volumes for the other silicate phases (wadsleyite, ringwoodite, orthoenstatite, low-pressure clinoenstatite, phase A, phase B and superhydrous B) are also very close (within about ±0.8% or better) to the

289 respective experimental values under ambient condition. We noticed by comparing calculations with different
290 pseudopotentials that good reproducibility of experimental cell parameters is important in order to achieve good
291 reproducibility of experimental NMR parameters.

292 The reported ^{1}H and ^{29}Si chemical shifts were calculated, respectively, using brucite (0.0 ppm with respective to
293 tetramethylsilane (TMS), Xue and Kanzaki (2009)) and Mg_2SiO_4 forsterite (-61.8 ppm with respective to
294 tetramethylsilane (TMS): data from this study, also see Stebbins 1995; Stebbins et al. 2009) as a secondary chemical
295 shift standard. The calculated isotropic ^{29}Si chemical shifts of tetrahedral Si and ^{1}H chemical shifts for the model
296 minerals are, respectively, within about ± 2 ppm and ±1 ppm (or better) of the corresponding experimental data (see
297 Table 1). This is broadly consistent with previous reports (generally within a few ppm) for various silicate and
298 phosphate phases (e.g., Ashbrook et al. 2007a; Ashbrook et al. 2007b; Charpentier 2011; Kanzaki and Xue 2012). It
299 should be noted that the agreement in isotropic chemical shift differences is in general better between similar local
300 structures. For example, between the two Si sites of phase A, Si2 site has a similar local structure to forsterite, with the
301 SiO_4 tetrahedron sharing both corners and edges with MgO_6 octahedra, whereas Si1 site shares only tetrahedral
302 corners with MgO_6 octahedra (Horiuchi et al. 1979; Kanzaki et al. 1992). When forsterite is chosen as a secondary ^{29}Si
303 chemical shift reference, the calculated isotropic chemical shift for the Si2 site of phase A (-64.0 ppm) is within 0.1
304 ppm of the corresponding experimental value (-63.9 ppm, Kanzaki et al. (1992)), whereas that of the Si1 site (-68.3
305 ppm) differs from the experimental value (-70.6 ppm) by a larger amount (~2 ppm). Agreements for octahedral Si
306 (e.g., Si1 sites in phase B and superhydrous B) are somewhat worse. Therefore, it is useful to choose a model structure
307 with local structures similar to those of the target phases as chemical shift reference. Forsterite and brucite have been
308 chosen for this reason. The calculated ^{1}H and ^{29}Si chemical shifts for the OH-bearing forsterite models are expected to
309 be reliable within about ±1 ppm or better, considering the lack of drastic variations in local structures.

310 In addition, to evaluate the relative stabilities of the different OH-bearing model structures (2 × 1 × 2 supercell) for
311 Mg_2SiO_4 forsterite under high pressure, which is more relevant to the sample synthesis condition, we also performed
312 additional DFT calculations to obtain the fully relaxed structure and enthalpy at a range of pressures from 0 to 12 GPa

313 (in step of 2 GPa). Enthalpy was calculated as the sum of internal energy (E) and a pressure (P) × volume (V) term.

314

315 **Simulation of NMR spectra from first-principles calculation results**

316 When protons are clustered (strongly dipolar coupled), both ^{1}H static and MAS NMR spectra are affected not
317 only by ^{1}H isotropic chemical shift, but also by the combined effect of ^{1}H homonuclear dipolar couplings (which are
318 dependent on the proton configurations) and chemical shift anisotropy (Maricq and Waugh 1979; Phillips et al. 1997;
319 Wu and Wasylishen 1993; Xue et al. 2008). In order to provide more direct comparison of the geometries and NMR
320 parameters from first-principles calculation with the experimental ^{1}H NMR spectra, we also simulated ^{1}H static and
321 MAS NMR powder spectra (at a ^{1}H resonance frequency of 400 MHz and spinning rates of 10-30 kHz) for the
322 calculated model structures and NMR chemical shielding tensors using the SIMPSON program (version 4.1.1) (Bak
323 et al. 2000). The ^{1}H-^{1}H dipolar couplings and the complete ^{1}H chemical shift tensors for all protons in the supercell
324 were included in the simulation. For the simulation of ^{1}H static NMR powder spectra, the direct method and ZCW
325 scheme (Cheng et al. 1973; Conroy 1967; Zaremba 1966)(using a large crystal file zcw28656.cry from the SIMPSON
326 website: http://nmr.au.dk/software/simpson/) for powder averaging of α and β angles were adopted. For ^{1}H MAS
327 NMR powder spectra, the γ-compute method (Hohwy et al. 1999) and REPULSION scheme (Bak and Nielsen 1997)
328 (crystal file rep168.cry in the SIMPSON program) were used. A Lorentzian line broadening function of 400 Hz was
329 applied to all the static NMR spectra and the MAS NMR spectra of the $(4H)_{Si}$ models; whereas a smaller Lorentzian
330 line broadening function of 50 Hz was applied to the MAS NMR spectra of the $(2H)_{Mg}$ models because of much
331 narrower line widths.

332

333 **Results**

334 **Raman spectra**

335 Unpolarized Raman spectra were taken on a number of grains for the hydrous forsterite sample. All the spectra
336 within the 200-1600 cm^{-1} region contain strong bands near 857 and 825 cm^{-1}, and weaker bands near 966, 920, 881,

608, 589, 546, 434, 374, 339, 331 and 305 cm^{-1} (not shown), consistent with those known for forsterite (e.g., Piriou and McMillan 1983). Note that the relative intensities vary between grains as a result of orientational dependency. Raman spectra within the O-H stretching region contain relative sharp bands near 3612, 3579 and 3567 cm^{-1} and a broader band near 3547 cm^{-1} (see Fig. 1 for an example), similar to previously reported Raman spectra for hydrous forsterite and Fe-bearing olivine synthesized at > 3 GPa (Bolfan-Casanova et al. 2014; Hushur et al. 2009; Manghnani et al. 2013). Peaks at similar positions have also been reported for infrared spectra of hydrous forsterite and Fe-bearing olivine synthesized at high pressure in numerous previous studies, and are generally agreed upon to be due to OH defects in the olivine structure (e.g., Bali et al. 2008; Berry et al. 2005; Kohlstedt et al. 1996; Kovacs et al. 2010; Lemaire et al. 2004; Mosenfelder et al. 2006; Otsuka and Karato 2011; Padrón-Navarta et al. 2014; Smyth et al. 2006). This suggests that water was indeed incorporated in the structure of forsterite in the present study.

^{1}H static and MAS NMR spectra

Figure 2 shows the fully relaxed ^{1}H static and MAS NMR spectra obtained at spinning rates of 10, 20 and 30 kHz (all with a recycle delay time of 60 s). The bulk water content was estimated from the total intensities of the ^{1}H MAS NMR spectra, and was found to be 0.45(1) wt%, in reasonable agreement with the nominal added water content (0.5 wt%). The quoted uncertainty represents the range of estimated values from NMR spectra obtained at different spinning rates.

The ^{1}H static NMR spectrum contains a narrower component on top of a broad component that span a chemical shift range of about 200 ppm (~80 kHz). The ^{1}H MAS NMR spectra also revealed two main components, a broader peak (full-width-at-half-maximum (FWHM) of 8.7 ppm and centered near 2.4 ppm at 30 kHz MAS) that has extensive spinning sidebands with asymmetric peak shapes and a narrower peak (FWHM of 1.1 ppm and centered at 1.2 ppm at 30 kHz MAS, contributing to about 1/4 of the total intensity) with much less prominent spinning sidebands. The former most likely corresponds to the broad component and the latter to the narrower component in the ^{1}H static NMR spectrum. In addition, the ^{1}H MAS NMR spectra also contain a very weak, even narrower peak near 7.3 ppm

(FWHM of 0.14 ppm at 30 kHz MAS, contributing to < 0.1% of the total intensity) (see Figs. 2-3, Table 2). All these components have a relatively long and similar ^{1}H spin-lattice relaxation time constant (T_1) of 10.6(6) s. There is also a very weak component centered near 5 ppm that has a significantly shorter T_1 than the other peaks. This is clear when the ^{1}H MAS NMR spectra taken with recycle delay times of 60 s and 3 s are compared (see Fig. 3): All the components except the small component near 5 ppm increase in intensity with increasing recycle delay time from 3 s to 60 s, whereas the extra component near 5 ppm has similar intensities, so that the difference spectrum of the two is free from such a component. It is known that water species absorbed on grain boundaries and in hydrous phases often have shorter ^{1}H T_1 than those in nominally anhydrous phases (Xue et al. 2006), and molecular water usually exhibits a peak near 4.8 ppm (Xue and Kanzaki 2004). Thus, it is highly likely that the minor extra component near 5 ppm is due to water present in grain boundaries. The contribution of this component to the total intensity is negligible. For the narrow component near 7.3 ppm, the narrowness of the peak and the relatively long ^{1}H T_1 suggest that it likely belongs to a crystalline phase. Its peak position does not agree with chemical shifts for known hydrous phases in the MgO-SiO_2-H_2O system. Judging from its similar ^{1}H T_1 to the main peaks, it is likely to be part of the forsterite structure. Kohn (1996; 2006) have also reported ^{1}H MAS NMR spectra obtained using a 200 MHz NMR spectrometer for two forsterite samples synthesized at 1.5 and 2.1 GPa under water-saturated condition. The reported spectra contain peaks near 1 ppm and 6.7 ppm (plus some additional narrow and broad peaks). Although it could not be excluded and most likely that these spectra include contributions from quenched hydrous phases and/or water in grain boundaries, the peak near 6.7 ppm and (part of) the peak near 1 ppm may correspond to the peaks near 7.3 and 1.2 ppm observed in the present study.

The broad component in the ^{1}H static and MAS NMR spectra of hydrous forsterite in Figure 2 resemble those of synthetic katoite ($Ca_3Al_2(H_4O_4)_3$) (Xue and Geiger, unpublished data; also see Cho and Rossman 1993; Cohen-Addad et al. 1964 for ^{1}H static NMR spectra). The broad component in the ^{1}H MAS NMR spectra also resemble that reported for a natural grossular garnet sample containing 3.6 wt% H_2O (Yesinowski et al. 1988). The grossular ($Ca_3Al_2(SiO_4)_3$) - katoite ($Ca_3Al_2(H_4O_4)_3$) solid solution series is well known to have a garnet structure, with each Si in the tetrahedral

site of grossular replaced by four hydrogen ions that are located near the face of the vacant tetrahedron toward the katoite composition (Lager et al. 1987; Lager et al. 1989). The close H-H distances among the four protons are largely responsible for the strong ^{1}H -^{1}H dipolar couplings and thus broad ^{1}H static and MAS peak widths. There is no corresponding narrow component, though, in the ^{1}H static and MAS NMR spectra of katoite.

2D ^{1}H NOESY NMR spectrum obtained at a spinning rate of 20 kHz and mixing times of 2 μs and 200 ms for the hydrous forsterite sample are shown in Figure 4. At a short mixing time of 2 μs, most of the intensities are along the diagonal (though broad for the very broad component near 2.4 ppm), whereas at a mixing time of 200 ms, cross peaks between the two main components are clearly developed. The increase in relative intensity for the cross peaks with mixing time confirms that the two components represent protons in close spatial proximity and thus must belong to the same phase. As a matter of fact, at a mixing time of 200 ms, spin diffusion has nearly reached equilibrium, as is clear from the similar peak shape for F2 cross sections at different positions of the F1 dimension (upper and middle cross sections in Fig. 4 at F1 peak positions with little and significant narrow component contribution, respectively). There are also a very weak and narrow peak near 7.3 ppm (lower cross sections in Fig. 4) and a weak and somewhat broader peak near 5 ppm, which do not show appreciable cross peaks with the two main peaks even at a mixing time of 200 ms, suggesting that these peaks represent protons more remote from the other protons. As described above, the component near 5 ppm has a shorter ^{1}H T_1 and is likely due to a small amount of protons (molecular water) from grain boundary materials; the narrow peak near 7.3 ppm has a ^{1}H T_1 similar to those of the main components and could be part of the forsterite structure, but more remote from the other protons.

2D ^{1}H CRAMPS-MAS NMR spectrum was also obtained at a spinning rate of 25 kHz with mixing times of 2 μs and 200 ms (Fig. 5). For the spectrum with a mixing time of 2 μs, the peak width in the CRAMPS dimension for the broad MAS component near 2.4 ppm is about 1 ppm, comparable to that of the narrower MAS component near 1.2 ppm (see the upper and middle cross sections in Fig. 5a). This suggests that the width of the broad peak in the MAS spectra is largely due to strong ^{1}H-^{1}H homonuclear dipolar couplings. Similar to the 2D NOESY spectra, at a mixing time of 200 ms, the two main components have nearly reached equilibrium as is clear from similar peak shapes for the

409 corresponding cross sections (upper and middle cross sections in Fig. 5b), whereas weaker peaks near 7.3 ppm and 5
410 ppm are distributed only along the diagonal.

411 Thus, the 1D and 2D ^{1}H NMR data revealed that there are two main populations of protons in the hydrous
412 forsterite structure, one experiencing strong ^{1}H-^{1}H homonuclear dipolar couplings and contributing to a broad peak
413 near 2.4 ppm, and another with weaker dipolar couplings and contributing to a narrower peak near 1.2 ppm
414 (accounting for about 1/4 of the total intensity) in the MAS NMR spectrum at 30 kHz. In addition, there is also a very
415 weak, narrow MAS NMR peak near 7.3 ppm (contributing to < 0.1% of the total intensity), most likely from more
416 remote protons in the forsterite structure.

417

418 **^{29}Si MAS and ^{1}H-^{29}Si CP-MAS NMR spectra**

419 The ^{29}Si MAS NMR spectrum obtained at a spinning rate of 20 kHz is shown in Figure 6. The spectrum is
420 dominated by a narrow peak near -61.7 ppm with a FWHM of 0.18 ppm, attributable to forsterite (Stebbins 1995).
421 There are also two very weak peaks near -80.6 and -83.2 ppm (each with an intensity of about 5% of the main peak),
422 attributable to a small amount of coexisting low-pressure clinoenstatite (Kanzaki et al. 1992, also see Table 1).

423 ^{1}H-^{29}Si CP-MAS NMR spectra acquired at a spinning rate of 20 kHz and contact times of 2, 4, 8 and 20 ms are
424 compared with the single-pulse ^{29}Si MAS NMR spectrum in Figure 7. Despite the large number of scans (7260-17920,
425 corresponding to about 30 to 75 hr of acquisition), the overall signal/noise ratios are relatively low, and the signal
426 intensities for all four contact times are not drastically different. Nevertheless, it is clear that compared to the ^{29}Si
427 single-pulse MAS spectrum that contains only a sharp peak near -61.7 ppm, additional peaks are also present in
428 the ^{1}H-^{29}Si CP-MAS NMR spectra: The latter includes a sharp, well resolved peak at a less negative chemical shift
429 (-60.9 ppm) and broader component(s) that encompass the chemical shift range of similar and more negative values
430 than the peak in the single-pulse MAS spectrum for forsterite. All four ^{1}H-^{29}Si CP-MAS NMR spectra can be
431 reasonably simulated by three mixed Gaussian-Lorentzian components with a common set of parameters: chemical
432 shift values of -60.9, -61.7 and -62.1 ppm and FWHM of 0.17, 0.42 and 0.45 ppm, respectively (see Fig. 8 and Table

433 2). The component near -61.7 ppm is close to the peak position for the single-pulse MAS spectrum, but is broader. The
434 higher-frequency peak near -60.9 ppm and the lower-frequency component near -62.1 ppm are most likely due to Si
435 sites in hydrous forsterite with local structures disturbed by the presence of OH defects.
436
437 **First-principles calculation results**
438 **Geometry and energy of optimized structures**. To gain better insights into the locations of protons in the
439 forsterite structure, we performed first-principles calculations on a number of model forsterite structures ($2 \times 1 \times 2$
440 supercell) with one Si atom replaced by four H atoms ($(4H)_{Si}$ models), or one Mg in an M1 or M2 site replaced by two
441 H atoms ($(2H)_{M1}$ and $(2H)_{M2}$ models) (see Table 3 and Figs. 9 and 10). Examples of the relaxed structures at 0 GPa
442 with the lowest energies for both types of substitutions are shown in Figure 9.
443 Before describing the forsterite structures containing OH defects, it is worthwhile to remind the reader of the
444 different types of oxygen and cation sites in the ideal olivine structure. There are three types of oxygen sites, O1, O2
445 and O3, with O1 and O2 located on a mirror plane, and O3 on a general position. Each oxygen is bonded to one Si and
446 three M cations. Each Si, which is located on a mirror plane, is bonded to two O3's and to one O1 and one O2.
447 Between the two types of M sites, M1 is located on an inversion center, and M2 on a mirror plane.
448 For the 4H for 1Si substitution ($(4H)_{Si}$ model), several previous first-principles calculation studies have reported the
449 energetics and geometries. Earlier studies generally reported optimized structures with the H on O1 migrated to the
450 exterior of the tetrahedron and the other three H ions staying close to tetrahedral edges or faces (Brodholt and Refson
451 2000; Verma and Karki 2009; Walker et al. 2007). More recently studies (Balan et al. 2011; Umemoto et al. 2011)
452 found that two geometries with one hydrogen bonded to O2 or O3 pointing away from the tetrahedral center give
453 lower energies. We have systematically tested several starting geometries for the four H positions, including those with
454 all four H atoms within the tetrahedron, and with one, two or three of the H atoms pointing away from the center of the
455 tetrahedron. Starting geometries with all four H atoms within the tetrahedron or with one H on O1 pointing away from
456 the tetrahedral center relaxed to (more than one) configurations in which three of the four H atoms (bonded to O2 and

O3's) are close to the tetrahedral edges or faces, and one (bonded to O1) is pointing out to the side of the tetrahedron, similar to those reported previously (Balan et al. 2011; Brodholt and Refson 2000; Umemoto et al. 2011; Verma and Karki 2009; Walker et al. 2007). Among these geometries, the one with the lowest energy (model 6) is shown in Figure 10. Geometries with one H bonded to O2 (model 1) or O3 (model 2), with two H atoms bonded to one O2 and one O3 (model 3) or to two O3's (model 4), and with three H atoms bonded to one O2 and two O3's (model 5), pointing away from the tetrahedral center were all found to be stable geometries. Geometries with one and three H atoms pointing away from the tetrahedral center are similar to those reported previously (Balan et al. 2011; Umemoto et al. 2011); those with two H atoms pointing away from the tetrahedral center were evaluated in this study for the first time. The relaxed structures at 0 GPa are shown in Figures 9 and 10, and the enthalpies of the relaxed structures at 0 and 12 GPa are compared in Table 3. At 0 GPa, the two structures with one H (bonded to either O2 or O3) pointing away from the center of the vacant tetrahedron (models 1 and 2) give similar and the lowest energies, consistent with those reported by Balan et al. (2011) and Umemoto et al. (2011). The geometry with the next-lowest energy (higher by 8.5 kJ/mol, 6.5 mRy, 0.088 eV than the above two) has two H atoms bonded to O2 and one of the two O3's pointing away from the center of the tetrahedron (model 3). The other geometries have even higher energies (by 20-36 kJ/mol, 15-28 mRy, 0.21-0.38 eV than the lowest-energy geometries). Thus, consistent with the calculation results of Balan et al. (2011) and Umemoto et al. (2011), the most likely geometries at 0 GPa are those with one H on O2 or O3 pointing away from the tetrahedral center (models 1 and 2 in Fig. 10). At 12 GPa, models 1 and 2 remain to be the lowest-enthalpy configurations (with model 2 being 3.6 kJ/mol higher), and models 3 to 6 have 19-63 kJ/mol higher enthalpies. Models 3 to 5 that contain two or three H atoms on O2 and/or O3 pointing away from the vacant tetrahedral center, in particular model 5 with three such H atoms, exhibit significantly larger enthalpy differences (from the lowest enthalpy of model 1) at high pressure as compared to 0 GPa, largely because of the PV term as a result of their larger volumes (see Table 3).

Therefore, the relative enthalpies at both 0 GPa and 12 GPa (and in between) suggest that the most possible configurations for the 4H for 1Si substitution ($(4H)_{Si}$) are models 1 and 2 with one H ion on O2 or O3 pointing away

481 from the tetrahedral center. This is in contrast to the well-known hydrogrossular ($Ca_3Al_2(SiO_4)_3$ - $Ca_3Al_2(H_4O_4)_3$)
482 substitution, in which all four H ions are known to be located close to the faces of the vacant tetrahedron and thus are
483 relatively close to one another (Lager et al. 1987; Lager et al. 1989). The difference is understandable, because in the
484 forsterite structure, interstitial octahedral sites adjacent to tetrahedral sites are available to accommodate the H ion(s) on
485 O2 or O3 pointing away from the tetrahedral center. Thus, such H ions, although substituting for Si in terms of charge
486 balance, are better regarded as residing in interstitial octahedral sites, rather than tetrahedral vacancies. There are two
487 types of interstitial octahedral sites in the olivine structure, I1 on an inversion center, and I2 on a mirror plane and
488 alternating with M2 sites along *c* direction (Walker et al. 2003). For all the $(4H)_{Si}$ models examined in this study, the H
489 ions on O2 or O3 pointing away from the tetrahedral center are located inside an interstitial site I2 (see Fig. 11), in
490 contrary to the claim by Umemoto et al. (2011). As will be discussed below, the presence of hydrogen ion(s) away
491 from the tetrahedral center has important consequence in terms of interpretations of ^{1}H NMR spectra, because such
492 protons are more remote from other protons (with inter-proton distances > 3 Å) and thus experience weaker ^{1}H-^{1}H
493 homonuclear dipolar couplings, compared to protons that are clustered in the vicinity of the vacant tetrahedron (near
494 tetrahedral edges with inter-proton distances of 1.80-1.93 Å for models 1 and 2). The two populations of protons with
495 stronger and weaker homonuclear dipolar couplings observed by ^{1}H NMR for hydrous forsterite may be explained by
496 the simulated configurations of 4H for 1Si substitution models, with the protons of weaker ^{1}H homonuclear dipolar
497 couplings corresponding to those pointing away from the vacant tetrahedral center.

498 For both of the models of 2H for 1Mg substitution in an M1 or M2 site, we have also searched for various
499 geometries. Similar to previous reports (Balan et al. 2011; Braithwaite et al. 2003; Brodholt and Refson 2000;
500 Umemoto et al. 2011; Verma and Karki 2009; Walker et al. 2007), we found that the lowest-energy geometry for 2H
501 for 1Mg substitution in an M1 site ($(2H)_{M1}$ model 1) has two H atoms that are related by inversion center and each
502 bonded to an O2 and hydrogen-bonded with an O1 (close to the O1-O2 octahedral edge), with O2-H, H···O1 and
503 O2-H···O1 distances of 1.013, 1.813 and 2.765 Å, respectively, and O2-H···O1 angle of 155.1° (Fig. 9b). The
504 lowest-energy geometry for 2H for 1Mg substitution in an M2 site ($(2H)_{M2}$ model 1) has each H bonded to a O3 and

505 hydrogen-bonded with another O3 (close to the O3-O3 octahedral edges), with H1 forming stronger hydrogen bond
506 (O3-H1, H1···O3' and O3-H1···O3' distances of 1.011, 1.926 and 2.832 Å, and O3-H1···O3' angle of 147.6°) than
507 H2 (O3-H2, H2···O3' and O3-H2···O3' distances of 0.991, 2.149 and 2.902 Å, and O3-H2···O3' angle of 131.5°).
508 The lowest-energy $(2H)_{M1}$ structure (model 1) is 63 and 79 kJ/mol lower in energy than the lowest-energy $(2H)_{M2}$
509 structure (model 1) at 0 GPa and 12 GPa, respectively (see Table 3), suggesting that if two H ions substitute for an Mg,
510 the most likely site is M1. This is again consistent with conclusions from previous theoretical calculations at 0 GPa
511 (Braithwaite et al. 2003; Brodholt and Refson 2000; Umemoto et al. 2011).

512 It is worth commenting on the hydrogen bonding distances in the $(4H)_{Si}$ and $(2H)_{Mg}$ models. Because tetrahedral
513 edges are shorter than M1 and M2 octahedral edges in defect-free olivine, it may be intuitive to think that hydrogen
514 ions substituting for Si experience stronger hydrogen bonding than those substituting for Mg. As a matter of fact, such
515 intuition led some authors to assign infrared O-H stretching bands with high frequencies (> 3450 cm^{-1}) to hydrogen
516 substituting for Mg, rather than Si (Hushur et al. 2009; Kudoh et al. 2006; Manghnani et al. 2013; Smyth et al. 2006).
517 However, Umemoto et al. (2011) pointed out from first-principles calculation for forsterite that hydrated tetrahedral
518 vacancies in fact have longer O-O tetrahedral edge lengths than those of occupied Si tetrahedra, and the order in O-O
519 edge length between a tetrahedral and an octahedral site is reversed for both unhydrated and hydrated vacancies due to
520 local relaxation around the vacancies. Blanchard et al. (2009) also noted the importance of local structure relaxation
521 around OH defects from first-principles calculation for Mg_2SiO_4 ringwoodite. We also observed similar trend for
522 forsterite in our calculation, but would like to note also the important role of strong hydrogen bonding interaction itself
523 in locally modifying the O-O edge length. For example, for the hydrated vacant tetrahedra in the two lowest-energy
524 $(4H)_{Si}$ models 1 and 2, all the O-O tetrahedral edge lengths (including those with and without an intervening hydrogen,
525 e.g. , 2.943-3.118 Å for O1-O2 and O1-O3 edges) are significantly lengthened as compared to those of defect-free
526 forsterite (2.763-2.773 Å for O1-O2 and O1-O3 edges) and occupied Si tetrahedra in the same model structures.
527 Hydrogen bonding is insignificant or weak for all these OH groups. On the other hand, for the hydrated vacant M1
528 octahedron in the lowest-energy $(2H)_{M1}$ model, all the O-O octahedral edges without an intervening hydrogen are

lengthened as compared to defect-free forsterite, whereas the strongly hydrogen bonded O2-H···O1 distance (2.765 Å) is significantly shorter compared to the O2- O1 edge length (3.026 Å) of defect-free forsterite and those of M1 sites occupied by Mg in the same model structure. The hydrogen bonding O-H···O distance thus does not simply reflect the O-O edge length of the defect-free structure or that of the relaxed vacancy, but is in fact largely affected by the hydrogen bonding interaction itself, which in turn is related to the local bonding environment of the OH group. Due to the isolated nature of SiO_4 tetrahedra in olivine, each OH associated with the $(4H)_{Si}$ defects is bonded only to three Mg cations, but not to any Si; whereas each OH associated with the $(2H)_{Mg}$ defects is bonded to one Si and two Mg cations. The contrast in hydrogen bonding strength between the two types of OH defects is in accord with the known trend that OH groups only bonded to metal cations (e.g., Mg, Ca) tend to form weak or no hydrogen bonding, whereas those bonded to a cation of high field strength (e.g., Si, P, S) tend to form moderate to strong hydrogen bonding, reflecting the difference in oxygen bond valence (Xue and Kanzaki 2004; Xue and Kanzaki 2009). Therefore, it would be misleading to use the average O-O edge lengths (or those of the defect-free crystal structure) determined by diffraction methods to infer the location of hydrogen in a nominally anhydrous mineral, because of local structural relaxation associated with the hydrogen bonding interaction as well as with cation vacancies. Instead, qualitative trend in hydrogen-bond forming tendency for OH groups in different bonding environments (bonded to cations of different field strength) could be useful in guiding interpretation of spectroscopic features that are closely related to hydrogen-bonding, such as ^{1}H chemical shift and O-H stretching frequency.

The calculated unit cell parameters for all the models at 0 GPa are compared with experimental data reported for anhydrous and hydrous forsterite under ambient condition in Table 4. Smyth et al. (2006) and Kudoh et al. (2006) have reported that water-bearing forsterite samples synthesized at 12 or 13.5 GPa give larger unit cell volumes than that of anhydrous forsterite under ambient condition. Smyth et al. (2006) further noted that the unit cell volume (V) may be expressed as a linear function of the water content (C_{H2O}): V (Å^3) = 290.107 + 0.55 * C_{H2O} (wt%) (with a correlation coefficient of 0.83). This would lead to a unit cell volume increase of 0.15% at a water content of 0.808 wt% for the $(2H)_{Mg}$ model, and 0.31% increase at a water content of 1.618 wt% for the $(4H)_{Si}$ model. Inspection of

553 Table 4 reveals that whereas the $(4H)_{Si}$ models 1 and 2 predict a volume increase of 0.30 and 0.36% respectively,
554 consistent with the experimental data, the $(2H)_{M1}$ model 1 predicts volume decrease (-0.07%), rather than increase,
555 with hydrogen incorporation. When the individual cell parameters are examined, the $(4H)_{Si}$ models 1 and 2 predict that
556 the increased cell volume is mainly due to increase in the *b* and *c* lengths, consistent with experimental data; whereas
557 the $(2H)_{M1}$ model 1 shows significant decrease in the *c* length and increase in both *a* and *b* lengths, inconsistent with
558 the reported experimental data. Thus, the reported unit cell parameters for water-bearing forsterite synthesized at 12
559 GPa (Smyth et al. 2006) are consistent with the $(4H)_{Si}$ models (1 and 2), rather than $(2H)_{M1}$ model, as the dominant
560 hydrogen incorporation mechanism. As the infrared and Raman spectra reported for these samples (Hushur et al.
561 2009; Smyth et al. 2006) show similar O-H stretching bands as the Raman spectra for forsterite in the present study,
562 the hydrogen incorporation mechanism must also be similar.

563 **^{1}H NMR results.** The calculated ^{1}H isotropic chemical shifts (δ_i^H) for all the OH-defect containing forsterite
564 models at 0 GPa are tabulated in Table 5. The $(4H)_{Si}$ models with 4H for 1Si substitution all yield small calculated ^{1}H
565 chemical shifts (-0.4 to 2.1 ppm for the two lowest-energy models 1 and 2). In contrast, models with 2H for 1Mg
566 substitution yield larger ^{1}H chemical shift (7.7 ppm for the lowest-energy $(2H)_{M1}$ model 1 in Fig. 9b). The difference in
567 ^{1}H chemical shift between the two types of OH defects is consistent with their difference in hydrogen-bonding
568 distances, which in turn reflects difference in their bonding environments (with the former bonded only to Mg cations,
569 and the latter also to a Si) as described above. Negative correlations between hydrogen-bonding (H···O and O-H···O)
570 distances and ^{1}H isotropic chemical shift are well known (Xue and Kanzaki 2009). Similarly, positive correlations
571 between hydrogen-bonding distances and O-H stretching frequency are also well known (Libowitzky 1999). The
572 relatively small ^{1}H chemical shifts for the two main peaks of the experimental ^{1}H MAS NMR spectra for hydrous
573 forsterite are consistent with their assignment to protons substituting for Si (and thus OH groups not bonded to any Si).
574 They are also expected to correspond to the relatively high-frequency O-H stretching vibrational bands (> 3450 cm^{-1})
575 observed in the Raman spectra. The very weak peak near 7.3 ppm is consistent with protons substituting for Mg (and
576 thus OH groups bonded to a Si). No corresponding low-frequency O-H stretching band is detected in the Raman

spectra, as is expected because of its negligible abundance. It most likely corresponds to the O-H stretching bands around 3160-3220 cm^{-1} reported by previous infrared studies of hydrous forsterite samples produced at < 3 GPa under high silica activity condition (e.g., Bali et al. 2008; Berry et al. 2005; Kovacs et al. 2010; Lemaire et al. 2004), as inferred earlier for a similar ^{1}H MAS NMR peak near 6.9 ppm for two forsterite samples synthesized at 1.5 and 2.1 GPa (Kohn 2006). The first-principles calculations of infrared spectra for similar model structures by Balan et al. (2011) and Umemoto et al. (2011) are in general consistent with these assignments of O-H stretching vibrational bands.

Because the peak shape of a ^{1}H NMR spectrum is affected not only by ^{1}H isotropic chemical shift, but also by ^{1}H homonuclear dipolar couplings and chemical shift anisotropy when protons are clustered (with short H-H distances), we also simulated ^{1}H static and MAS powder NMR spectra for all the model structures using the SIMPSON program (Bak et al. 2000) to facilitate better comparison with experimental data.

The simulated ^{1}H static and MAS NMR spectra (20 kHz spinning rate) for the lowest-energy models of 4H for 1Si substitution ($(4H)_{Si}$ models 1 and 2) and 2H for 1Mg (M1) substitution ($(2H)_{M1}$ model 1) are compared with the corresponding experimental spectra in Figures 12 and 13. The simulated ^{1}H static and MAS NMR spectra for all other models can be found in the supplementary Figures 1 and 2. For both the static and MAS NMR spectra, the two main components are well reproduced by both of the two $(4H)_{Si}$ models (1 and 2) with one H pointing away from the tetrahedral center: the narrow component (of about 1/4 of the total intensity) is due to the proton pointing away from the tetrahedral center, and the broad component is dominantly due to the other protons that are clustered near the vacant tetrahedron (along tetrahedral edges). Note that even the asymmetric peak shape of the spinning sidebands in the ^{1}H MAS NMR spectra are reproduced. The broadness and complicated peak shapes are due to the combined effect of strong ^{1}H multi-spin homonuclear dipolar couplings and chemical shift anisotropy, which are 'homogeneous' interactions that cannot be completely eliminated unless spinning at very fast spinning rates (Maricq and Waugh 1979). Model 6, which has all protons in the vicinity of the vacant tetrahedron (within 1.62-2.37 Å of one another), gives a broad component for both the static and MAS spectra that resemble the corresponding broad component observed for

601 hydrous forsterite, but yields no corresponding narrow component. The other models, which have two or three protons
602 (on O2 and/or O3) pointing away from the vacant tetrahedral center (models 3, 4, and 5), on the other hand, cannot
603 account for the observed broad component in both the static and MAS spectra of the hydrous forsterite sample.
604 The simulated spectrum for the $(2H)_{M1}$ model 1 gives a narrow MAS NMR peak with a larger ^{1}H isotropic
605 chemical shift, matching well with the very weak peak at 7.3 ppm in the experimental ^{1}H MAS NMR spectra. The
606 narrowness of the peak in the simulated MAS NMR spectrum is because the two protons are magnetically equivalent
607 (related by an inversion center). It is well known that when two spins are magnetically equivalent, homonuclear
608 dipolar couplings between them become 'inhomogeneous' interactions, which are completely eliminated by sample
609 spinning at the magic angle (Maricq and Waugh 1979). The H-H distance (2.54 Å) for the $(2H)_{M1}$ model 1 is also
610 longer than the shorter population of H-H distances (1.80-1.93 Å) for the lowest-energy $(4H)_{Si}$ models 1 and 2. The
611 $(2H)_{M2}$ model 1 gives two narrow peaks near 7.4 and 5.9 ppm in the MAS NMR spectra. Considering its significantly
612 higher energy, this model is less likely than the $(2H)_{M1}$ model.
613 Thus, both qualitative consideration of the relative H-H proximity and ^{1}H chemical shift, and quantitative
614 simulation of the ^{1}H static and MAS NMR spectra strongly support that the main components (broad and narrower
615 peaks, near 2.4 and 1.2 ppm in the case of MAS spectra) observed for hydrous forsterite by ^{1}H NMR measurements
616 can be attributed to protons substituting for Si, most likely corresponding to $(4H)_{Si}$ models 1 and 2, and the very minor,
617 narrow peak near 7.3 ppm in the ^{1}H MAS NMR spectra can be attributed to trace amount of protons substituting for
618 Mg in M1 sites. The reasonable agreement between the experimental ^{1}H NMR spectra and those calculated based on
619 model structures (that have fixed proton positions) also implies that proton exchanges between the two main
620 components due to dynamic motion are insignificant at room temperature in the NMR time scale.
621 **^{29}Si NMR results.** The calculated ^{29}Si isotropic chemical shifts for all the OH-defect containing forsterite models
622 are tabulated in Table 6. Before discussing these calculation results, a brief reminder of the local structures of forsterite
623 is rewarding. In forsterite, the isolated SiO_4 tetrahedra are linked to M1 and M2 octahedra by edge and corner sharing.
624 Each M1 octahedron is linked to two SiO_4 tetrahedra by edge sharing and to two SiO_4 tetrahedra by corner sharing;

each M2 octahedron is linked to one SiO_4 tetrahedron by edge sharing and to four SiO_4 tetrahedra by corner sharing.

It is well known that NMR parameters are affected increasingly less by more distant neighbors (Stebbins and Xue 2014). Consistent with this, for the $(2H)_{M1}$ model 1, the four Si sites that are linked to the vacant M1 site have greater differences in ^{29}Si chemical shift (δ_i^{Si}) (two by 1.6 ppm and two by -3.7 ppm) from that of defect-free forsterite structure; all the other Si sites in the supercell have much smaller δ_i^{Si} differences from defect-free forsterite (-0.1 to 0.4 ppm with an average close to 0 ppm). The -3.7 ppm difference in δ_i^{Si} from defect-free forsterite corresponds to the two Si tetrahedra that each share an edge (O2-O3) with the vacant octahedron (with O2 bonded to a H forming SiOH linkage); the 1.6 ppm difference corresponds to the two Si tetrahedra that each share a corner (O1) with the vacant M1 octahedron.

For the $(2H)_{M2}$ model 1, the five Si tetrahedra that are directly linked to the vacant M2 octahedron have greater differences in δ_i^{Si} from defect-free forsterite (2.4, 1.3, -0.7, -1.8 and -5.0 ppm); all the other Si sites in the supercell have small δ_i^{Si} differences (-0.2 to 0.4 ppm with an average close to 0 ppm). For the former, there are no obvious correlations between δ_i^{Si} and the type of linkage with the vacant M2 site (edge or corner sharing) or the type of shared oxygen (whether bonded to a H forming SiOH linkage or not) (see Table 6).

For the $(4H)_{Si}$ models, because the vacant Si tetrahedron is not directly linked to other Si tetrahedra, the influence on ^{29}Si chemical shift for most Si are very small. Exceptions occur when a proton is pointing away from the vacant tetrahedral center and located in an adjacent interstitial octahedral site (models 1 to 5), because the proton is then close to an adjacent Si (with relatively short Si-H distances of 2.35-2.56 Å). For Si close to a proton pointing away from the tetrahedral center and bonded to O3 (Si11 in model 2, Si10 in model 3, and Si10 and Si11 in models 4 and 5), the ^{29}Si chemical shifts all differ from that of defect-free forsterite by about 1.6 ppm. Whereas for Si close to a proton pointing away from the tetrahedral center and bonded to O2 (Si13 in models 1, 3 and 5), the difference in chemical shift from defect-free forsterite is small (~0.3 ppm). All the other Si in the supercell give ^{29}Si chemical shift differences in the range of -1.0 to 0.8 ppm (-0.6 to 0.5 ppm for the two lowest-energy models 1 and 2) with an average close to 0 ppm.

As discussed above, for the ^{1}H-^{29}Si CP-MAS NMR spectra of hydrous forsterite, two peaks are observed, one

649 narrower and well-resolved peak near -60.9 ppm (about 0.8 ppm from the peak of OH-free forsterite as detected by
650 single-pulse ^{29}Si MAS NMR); another broader peak close to the position for OH-free forsterite, which may be further
651 decomposed into two components near -61.7 ppm and -62.1 ppm (about 0 and -0.4 ppm from the peak of OH-free
652 forsterite). The former peak would be consistent with Si adjacent to a proton that is bonded to O3 and pointing away
653 from the tetrahedral center in the $(4H)_{Si}$ models (e.g., Si11 in the lowest-energy model 2), and the latter are consistent
654 with all $(4H)_{Si}$ models, including the lowest-energy model 1. $(2H)_{M1}$ and $(2H)_{M2}$ models will result in peaks with
655 greater shifts from that of OH-free forsterite, and most likely do not significantly contribute to the observed peaks in
656 the ^{1}H-^{29}Si CP-MAS NMR spectra of hydrous forsterite. Thus, the ^{1}H-^{29}Si CP-MAS NMR and ^{1}H NMR data of
657 hydrous forsterite together can be taken to be consistent with the lowest-energy $(4H)_{Si}$ models 1 and 2, with at least
658 some of the $(4H)_{Si}$ defects having the configuration of model 2 (with the proton pointing away from the vacant
659 tetrahedral center bonded to O3).
660

661 **Discussion**

662 **NMR and vibrational spectroscopic characteristics of OH defects in hydrous forsterite**

663 The first-principles calculation and ^{1}H and ^{29}Si NMR measurements in this study suggest that different OH defects
664 in hydrous forsterite can be unambiguously distinguished by ^{1}H and ^{29}Si NMR. The most plausible configurations of
665 the 4H for 1Si substitution in forsterite ($(4H)_{Si}$ models 1 and 2) have one H ion on O2 or O3 pointing away from the
666 tetrahedral center and located inside an interstitial octahedral site I2. They are characterized by relatively small ^{1}H
667 isotropic chemical shifts, and coexistence of protons with weak and strong dipolar couplings, resulting in two
668 components in both ^{1}H static and MAS NMR spectra: a narrower component corresponding to protons pointing away
669 from the tetrahedral center, and a broader component corresponding to the remaining protons that are clustered in the
670 vicinity of the vacant tetrahedra (along tetrahedral edges). These two components (centered near 1.2 and 2.4 ppm,
671 respectively, at 30 kHz MAS) constitute the dominant proton species in the ^{1}H NMR static and MAS NMR spectra of
672 hydrous forsterite synthesized at 12 GPa and 1200 °C in this study. The ^{1}H-^{29}Si CP-MAS NMR measurements

673 revealed peaks shifted from that of OH-free forsterite, with a narrower peak exhibiting a positive shift of about 0.8
674 ppm, and a broader peak encompassing the range of little and smaller negative shifts. The former may be attributed to
675 Si in the vicinity of a proton pointing away from the vacant tetrahedral center and bonded to O3 ($(4H)_{Si}$ model 2), and
676 the latter to Si in the vicinity of other protons associated with $(4H)_{Si}$ defects (including model 1) on the basis of
677 first-principles calculation result.

678 We also observed a very weak and even narrower peak near 7.3 ppm in the ^{1}H MAS NMR spectra of hydrous
679 forsterite. This matches well with the calculated ^{1}H chemical shift and peak width (free from broadening due to dipolar
680 couplings) for the substitution of 2H for 1Mg in an M1 site of forsterite ($(2H)_{M1}$ model 1). The significantly larger ^{1}H
681 chemical shift for protons associated with the $(2H)_{M1}$ model than the $(4H)_{Si}$ models is correlated with the stronger
682 hydrogen bonding for the former, which in turn reflects difference in bonding environments of the OH groups (with
683 the former bonded to a Si, and the latter only bonded to Mg). The first-principles calculation also predicts two ^{29}Si
684 NMR peaks shifted from that of defect-free forsterite by 1.6 and -3.7 ppm associated with the $(2H)_{M1}$ defect. We did
685 not observe peaks assignable to such Si in the ^{1}H-^{29}Si CP-MAS NMR spectra, which is unsurprising because of its
686 low concentration. These ^{1}H and ^{29}Si NMR characteristics can be used to identify and quantify the different types of
687 OH defects in hydrous forsterite.

688 The Raman spectra for the forsterite sample in this study contain four major high-frequency O-H stretching
689 vibrational bands near 3612, 3579, 3567 and 3547 cm^{-1}, similar to previously reported Raman and infrared spectra for
690 hydrous forsterite synthesized at high pressure (e.g., Bali et al. 2008; Bolfan-Casanova et al. 2014; Lemaire et al. 2004;
691 Smyth et al. 2006). As there is a negative correlation between ^{1}H chemical shift and O-H stretching frequency (Xue
692 and Kanzaki 2009), these high O-H stretching frequencies are consistent with $(4H)_{Si}$ defects, as was confirmed by
693 first-principles calculations (Balan et al. 2011; Umemoto et al. 2011). The dominance of protons associated with $(4H)_{Si}$
694 defects as revealed by ^{1}H and ^{29}Si NMR is also in supportive of such an assignment. Although trace amount of protons
695 associated with $(2H)_{M1}$ defects was identified by ^{1}H MAS NMR, no corresponding bands in the Raman spectra are
696 observed because of its low abundance. They are expected to give low O-H stretching frequencies near 3160-3220

697 cm^{-1}, from the known negative correlation between ^{1}H chemical shift and O-H stretching frequency, and from
698 previous first-principles calculation results for the $(2H)_{M1}$ model (Balan et al. 2011; Umemoto et al. 2011) and infrared
699 spectroscopic data for forsterite samples synthesized at different pressure and silica activity conditions (e.g., Bali et al.
700 2008; Berry et al. 2005; Kovacs et al. 2010; Lemaire et al. 2004).

701 As outlined in the Introduction, despite convincing evidence for the high-frequency character of O-H stretching
702 bands for $(4H)_{Si}$ defects from previous first-principles calculations, detailed assignment for experimentally observed
703 O-H stretching bands in this region, especially regarding the nature of one major band near 3550 cm^{-1}, for forsterite
704 (and olivine in general) remained not well constrained. Our study may shed new light on this.

705 A previous low-temperature infrared study by Ingrin et al. (2013) on a hydrous forsterite sample postulated that two
706 O-H stretching bands, including one near 3550 cm^{-1} at room temperature (near 3566 cm^{-1} at -194 °C), could be due to
707 (charged) H ions in interstitial positions because they exhibit stronger temperature-dependent frequency and peak
708 width changes than other O-H stretching bands above 3450 cm^{-1}. A subsequent first-principles calculation study by
709 Balan et al. (2014) further proposed that the broad band near 3550 cm^{-1} may be due to a (charged) interstitial OH
710 group next to a five-coordinate Si. This band is ubiquitously observed in hydrous olivine synthesized at relatively high
711 pressure, accounting for about 1/4 of the total intensities (cf. Ingrin et al. 2013), and is also clearly observed in the
712 Raman spectra from this study. If a quarter of the protons are associated with five-coordinate Si, a ^{29}Si NMR peak due
713 to the latter should be readily observable (likely with intensity of similar order of magnitude compared to those for Si
714 associated with $(4H)_{Si}$ defects) in ^{1}H-^{29}Si CP-MAS NMR spectra. However, no peaks in the region expected for
715 five-coordinate Si (around -124 to -150 ppm: Stebbins and Xue 2014; Xue et al. 2010) were observed in the ^{1}H-^{29}Si
716 CP-MAS NMR spectra of this study (not shown). Considering that charged defects are in general energetically less
717 favorable than neutral defects, it is doubtful that they could be present at such high abundance. Instead, as detailed
718 below, the observed O-H stretching band near 3550 cm^{-1} could be simply associated with neutral $(4H)_{Si}$ defects that
719 have one proton pointing away from the vacant tetrahedral center and located in an adjacent interstitial site.

720 Ingrin et al. (2013) postulated (charged) H atoms in interstitial positions to explain O-H stretching bands of greater

721 anharmonicity on the assumption that vibrational bands corresponding to a given defect should exhibit similar
722 anharmonic properties. However, there is no compelling evidence to support this assumption. Even for neutral $(4H)_{Si}$
723 defects, the proton pointing away from the vacant tetrahedral center and located in an adjacent interstitial site has a
724 different local environment compared to the remaining protons, and thus could have different proton dynamics. Balan
725 et al. (2011) has reported H atomic displacement for the O-H stretching normal modes of $(4H)_{Si}$ models (Si_3 and
726 Si_4), similar to the lowest-energy models 1 and 2 in this study, from first-principles calculation. Inspection of their
727 results reveals that the O-H stretching vibration of the O-H bond pointing away from the tetrahedral center is in fact not
728 strongly coupled with those of other O-H bonds, and dominantly contributes to a normal mode near 3572 cm^{-1} for
729 model Si_3 and near 3402 cm^{-1} for model Si_4, respectively. These two normal modes both have strong intensities
730 along *a* and *b* directions in the calculated polarized infrared spectra. The experimentally observed band near 3550 cm^{-1}
731 has been reported to exhibit the strongest intensity along *b* and lower but significant intensity along *a* in polarized
732 infrared spectra (cf. Ingrin et al. 2013), in reasonable though not perfect agreement with those calculated for the two
733 normal modes. The normal mode near 3572 cm^{-1} for model Si_3 (model 1 in this study) could, in particular,
734 correspond to the experimentally observed band near 3550 cm^{-1}, given its better agreement in frequency. In fact, Ingrin
735 et al. (2013) has already pointed out that the other three major experimentally observed O-H stretching bands match
736 reasonably well with three of the four calculated bands of model Si_3 by Balan et al. (2011) in terms of both frequency
737 and pleochroic property (with the band near 3612 cm^{-1} polarized along *a*, the band near 3579 cm^{-1} polarized along both
738 *a* and *b*, and the band near 3567 cm^{-1} polarized along *c* in polarized infrared spectra), but they could not readily assign
739 the fourth calculated band to any major observed band. The attribution of the experimentally observed major band
740 near 3550 cm^{-1} to the same $(4H)_{Si}$ model would provide the last missing piece of the puzzle.

741 Therefore, the major O-H stretching bands observed near 3612, 3579, 3567 and 3550 cm^{-1} at room temperature
742 (near 3614, 3581, 3568 and 3566 cm^{-1} at -194 °C according to Ingrin et al. 2013) in Raman and infrared spectra of
743 hydrous forsterite could correspond to the four normal modes of $(4H)_{Si}$ model 1 in this study, with calculated
744 frequencies (at 0 K) of 3591, 3540, 3520, and 3572 cm^{-1} by Balan et al. (2011) and 3626, 3572, 3554 and 3612 cm^{-1}

by Umemoto et al. (2011). The $(4H)_{Si}$ model 2 (of similar calculated enthalpy) has been reported to give calculated O-H stretching frequencies of 3555, 3512, 3494 and 3402 cm^{-1} by Balan et al. (2011), and 3589, 3541, 3525 and 3433 cm^{-1} by Umemoto et al. (2011). It could contribute to some other weaker O-H stretching bands in the high-frequency region (e.g., near 3480 cm^{-1}), which have often been observed in previous infrared and Raman studies of hydrous forsterite (e.g., Bali et al. 2008; Bolfan-Casanova et al. 2014; Kovacs et al. 2010; Lemaire et al. 2004; Smyth et al. 2006), but were not detected by Raman in this study possibly due to poor signal/noise. The vibrational spectroscopic data are thus in complete agreement with the conclusion derived from ^{1}H and ^{29}Si NMR data, and together suggest that $(4H)_{Si}$ defects corresponding to both of the two lowest-energy models 1 and 2 (with one hydrogen on O2 and O3, respectively, pointing away from the tetrahedral center) are present in the hydrous forsterite structure. There is no need to invoke charged interstitial OH groups to explain the observed O-H stretching bands.

In note by passing for completeness, for olivine samples containing Fe^{2+}, Fe^{3+} and other trace elements, additional O-H stretching vibrational bands associated with these cations might be expected in vibrational spectra (e.g., 3572 and 3525 cm^{-1} associated with Ti^{4+}; one or more bands between 3300 and 3400 cm^{-1} associated with trivalent cations such as Fe^{3+}, Cr^{3+}) (Balan et al. 2011; Berry et al. 2005; Berry et al. 2007).

Hydrogen incorporation mechanisms in forsterite as a function of pressure and composition

Our study has unambiguously confirmed that the dominant hydrogen incorporation mechanism in forsterite at 12 GPa is hydrogarnet-like with 4H substituting for 1Si in a tetrahedral site, but unlike hydrogarnet with unique configurations of one proton on O2 or O3 pointing away from the vacant tetrahedral center and located inside an interstitial octahedral site. Protons substituting for Mg in an M1 site were also detected, but at very low concentration (< 0.1% of the total content). The detection of the latter by ^{1}H MAS NMR in our sample was largely a result of greater sensitivity because it has a much narrower peak width than protons substituting for Si.

The spectroscopic characteristics for the different OH defects in hydrous forsterite described in the previous section can be used to systematically reexamine the incorporation mechanisms of hydrogen in Mg_2SiO_4 forsterite (and

769 $(Mg,Fe)_2SiO_4$ olivine) under a wider range of pressure and chemical conditions, by inspecting infrared and Raman
770 data reported thus far. Previously reported infrared and Raman data for hydrous forsterite (and often also
771 $(Mg,Fe)_2SiO_4$ olivine) synthesized at a range of pressures above 3 GPa (e.g., Bali et al. 2008; Kohlstedt et al. 1996;
772 Mosenfelder et al. 2006; Otsuka and Karato 2011; Smyth et al. 2006; Withers et al. 2011) can now be interpreted
773 consistently, with the new guide described above, as suggesting the $(4H)_{Si}$ defects being the dominant species,
774 regardless of silica activity, because the spectra are generally dominated by high-frequency O-H stretching bands >
775 3450 cm^{-1}. A weak, low-frequency O-H stretching band near 3160 cm^{-1}, attributable to the $(2H)_{M1}$ defects, is also
776 visible in the infrared spectra for some of these samples, e.g. forsterite samples (enstatite-buffered) synthesized at 6 and
777 9 GPa by Bali et al. (2008). These results are in general consistent with the present study, suggesting that the $(4H)_{Si}$
778 defects are the dominant species, but the $(2H)_{M1}$ defects may exist in minor amounts at > 3 GPa.
779 Previously reported infrared data for hydrous forsterite (and $(Mg,Fe)_2SiO_4$ olivine) produced at lower pressures (<
780 3 GPa) (e.g., Bali et al. 2008; Berry et al. 2005; Demouchy and Mackwell 2003; Grant et al. 2006; Lemaire et al. 2004;
781 Padrón-Navarta et al. 2014) can now be (re-)interpreted as indicating variation in the proportion of the two types of
782 OH defects with silica activity, with low silica activity favoring the $(4H)_{Si}$ defects and high silica activity favoring the
783 $(2H)_{M1}$ defects, although quantitatively there are inconsistencies among different studies in the relative intensities.
784 Because of the high sensitivity of ^1H MAS NMR in detecting the very narrow peak due to protons associated with the
785 $(2H)_{M1}$ defects, and the quantitative nature of NMR spectroscopy (without the need for frequency- or site- dependent
786 calibration factor as required by infrared spectroscopy), it would be useful in the future to conduct a systematic NMR
787 study on hydrous forsterite samples synthesized at a range of pressures and silica activities to better quantify the
788 pressure and compositional dependency of the two hydrogen incorporation mechanisms in forsterite.
789

790 **Implications**

791 The effect of hydrogen incorporation on mineral properties, such as diffusivity, electrical conductivity and
792 mechanical strength, are expected to strongly depend on how hydrogen ions are incorporated in the crystal structure. A

793 previous theoretical calculation has evaluated the migration barriers for proton from magnesium vacancy to interstitial
794 sites and from interstitial to interstitial sites for forsterite, but did not consider migration from Si vacancies because of
795 "the very large energy barriers associated with Si vacancy" (Verma and Karki 2009). However, the $(4H)_{Si}$ model
796 considered in that study has a configuration with the H on O1 migrated to the exterior of the vacant tetrahedron and
797 those on O2 and O3's staying on the tetrahedral faces. Our study, as well as the recent studies by Balan et al. (2011)
798 and Umemoto et al. (2011), has revealed that this is not the lowest-energy configuration, and the most plausible
799 configurations, instead, have one hydrogen (on O2 or O3) pointing away from the vacant tetrahedral center and
800 located inside an adjacent interstitial octahedral site. It is worth further theoretical calculation to investigate whether the
801 positioning of one proton of the $(4H)_{Si}$ defect in an interstitial octahedral site could yield lower-energy barriers for
802 proton migration and provide a favorable path for proton diffusion in olivine.

803 Despite diverse interpretations in the literature, the dominance of protons associated with Si vacancies in olivine
804 at relatively high pressure (> 3 GPa) implies that such protons should be largely responsible for the observed reduction
805 of mechanical strength (Hirth and Kohlstedt 2003), Si diffusivities (Costa and Chakraborty 2008; Fei et al. 2013) and
806 electrical conductivities (Dai and Karato 2014a; Dai and Karato 2014b; Poe et al. 2010; Wang et al. 2006; Yoshino et
807 al. 2009) of olivine associated with hydrogen incorporation within the corresponding pressure range. For example, for
808 the electrical conductivity data of olivine, although the $(2H)_{Mg}$ defect has often been envisioned (Karato 1990; Karato
809 2013; Karato 2015), almost all the samples of electrical conductivity measurements can now be (re-)interpreted as
810 dominated by $(4H)_{Si}$ defects, judging from the reported infrared spectra (with dominantly high-frequency O-H
811 stretching bands > 3450 cm^{-1}) (Dai and Karato 2014a; Dai and Karato 2014b; Poe et al. 2010; Wang et al. 2006;
812 Yoshino et al. 2009). Atomistic interpretations of physical properties based on structural information from
813 spectroscopic observations are desirable. It is also worth mentioning that although the $(2H)_{Mg}$ defects detected in our
814 study is minor, and is in general expected to be a less important hydrogen incorporation mechanism in olivine at high
815 pressure (> 3 GPa), its concentration is likely greater than that of intrinsic Mg vacancies, and thus could still play a
816 non-negligible role for Mg diffusion in olivine containing OH defects.

817 At pressures < 3 GPa, as described above, the limited available infrared spectroscopic data in the literature can
818 now be (re-)interpreted as showing dependency of the OH defects on silica activity, with the $(2H)_{Mg}$ defects playing a
819 greater role at high silica activity. There have been few electrical conductivity measurements at such pressure range,
820 although a H-D inter-diffusion experiment for a natural San Carlos olivine conducted at 2 GPa (buffered by enstatite)
821 (Du Frane and Tyburczy 2012) has often been evoked to explain electrical conductivity results obtained at higher
822 pressures (e.g., Karato 2013; Karato 2015). The study of Du Frane and Tyburczy (2012) did not report any infrared or
823 Raman spectra to directly reveal the hydrogen incorporation mechanism. If the trend of silica activity dependency
824 reported thus far is robust, one would expect samples of Du Frane and Tyburczy (2012) to be dominated by $(2H)_{Mg}$
825 defects. On the other hand, samples of electrical conductivity measurements reported thus far at higher pressures are
826 dominated by $(4H)_{Si}$ defects, as described above, and thus the H-D inter-diffusion result of Du Frane and Tyburczy
827 (2012) might not be directly applicable. Clearly, more systematic studies on both hydrogen incorporation mechanisms
828 and physical properties, ideally with all samples used for the latter carefully characterized by spectroscopy for OH
829 speciation, at a range of pressures and compositions are desirable.
830 Finally, our study demonstrated that the combined careful ^{1}H and ^{29}Si NMR measurements and first-principles
831 calculation approach is very effective in revealing the detailed hydrogen incorporation mechanism in nominally
832 anhydrous minerals. We are in the process of investigating other important nominally anhydrous mantle minerals
833 (including higher-pressure polymorphs of olivine (wadsleyite, ringwoodite), enstatite and grossular) using a similar
834 approach to gain greater insights into the general principles governing hydrogen incorporation in silicate minerals. The
835 combined solid-state NMR and first-principles calculation approach should also be effective for the study of hydrogen
836 incorporation (and other structural aspects) in other inorganic materials.
837
838 **Acknowledgements.** We are grateful to Istvan Kovacs (associate editor), Simon Kohn and an anonymous
839 reviewer for helpful comments and suggestions. Part of this study was carried out during the Misasa International
840 Student Intern Program 2015 (participated by D.T. & D. L.), which was supported by a "Special Expenditure" funded

841 by the Ministry of Education, Culture, Sports, Science and Technology of Japan. We thank Yusuke Yachi and
842 Tsutomu Ota for assistance with EPMA analysis.

843

844 **References Cited**

845 Ashbrook, S.E., Le Polles, L., Pickard, C.J., Berry, A.J., Wimperis, S., and Farnan, I. (2007a)
846 First-principles calculations of solid-state ^{17}O and ^{29}Si NMR spectra of Mg_2SiO_4 polymorphs.
847 Physical Chemistry Chemical Physics, 9, 1587-1598.
848 Ashbrook, S.E., Berry, A.J., Frost, D.J., Gregorovic, A., Pickard, C.J., Readman, J.E., and Wimperis, S.
849 (2007b) ^{17}O and ^{29}Si NMR parameters of $MgSiO_3$ phases from high-resolution solid-state NMR
850 spectroscopy and first-principles calculations. Journal of the American Chemical Society, 129,
851 13213-13224.
852 Bai, Q., and Kohlstedt, D.L. (1992) Substaintial hydrogen solubility in olivine and implications for water
853 storage in the mantle. Nature, 357, 672-674.
854 --- (1993) Effects of chemical environment on the solubility and incorporation mechanism for hydrogen
855 in olivine. Physics and Chemistry of Minerals, 19, 460-471.
856 Bak, M., and Nielsen, N.C. (1997) REPULSION, A Novel Approach to Efficient Powder Averaging in
857 Solid-State NMR. Journal of Magnetic Resonance, 125, 132-139.
858 Bak, M., Rasmussen, J.T., and Nielsen , N.C. (2000) SIMPSON: A General Simulation Program for
859 Solid-State NMR Spectroscopy Journal of Magnetic Resonance, 147, 296-330.
860 Balan, E., Ingrin, J., Delattre, S., Kovacs, I., and Blanchard, M. (2011) Theoretical infrared spectrum of
861 OH-defects in forsterite. European Journal of Mineralogy, 23, 285-292.
862 Balan, E., Blanchard, M., Lazzeri, M., and Ingrin, J. (2014) Contribution of interstitial OH groups to the
863 incorporation of water in forsterite. Physics and Chemistry of Minerals, 41, 105-114.
864 Bali, E., Bolfan-Casanova, N., and Koga, K.T. (2008) Pressure and temperature dependence of H

865 solubility in forsterite: An implication to water activity in the Earth interior. Earth and Planetary
866 Science Letters, 268, 354-363.
867 Berry, A.J., Hermann, J., O'Neill, H.S.C., and Foran, G.J. (2005) Fingerprinting the water site in mantle
868 olivine. Geology, 33, 869-872.
869 Berry, A.J., O'Neill, H.S.C., Hermann, J., and Scott, D.R. (2007) The infrared signature of water
870 associated with trivalent cations in olivine. Earth and Planetary Science Letters, 261, 134-142.
871 Bielecki, A., Kolbert, A.C., and Levitt, M.H. (1989) Frequency-switched pulse sequences: homonuclear
872 decoupling and dilute spin NMR in solids. Chemical Physics Letters, 155, 341-346.
873 Blanchard, M., Balan, E., and Wright, K. (2009) Incorporation of water in iron-free ringwoodite: A
874 first-principles study. American Mineralogist, 94, 83-89.
875 Bolfan-Casanova, N., Montagnac, G., and Reynard, B. (2014) Measurement of water contents in olivine
876 using Raman spectroscopy. American Mineralogist, 99, 149-156.
877 Braithwaite, J.S., Wright, K., and Catlow, C.R.A. (2003) A theoretical study of the energetics and IR
878 frequencies of hydroxyl defects in forsterite. Journal of Geophysical Research-Solid Earth, 108,
879 2284.
880 Brodholt, J.P., and Refson, K. (2000) An ab initio study of hydrogen in forsterite and a possible
881 mechanism for hydrolytic weakening. Journal of Geophysical Research-Solid Earth, 105,
882 18977-18982.
883 Brown, S.P. (2007) Probing proton-proton proximities in the solid state. Progress in Nuclear Magnetic
884 Resonance Spectroscopy, 50, 199-251.
885 Charpentier, T. (2011) The PAW/GIPAW approach for computing NMR parameters: A new dimension
886 added to NMR study of solids. Solid State Nuclear Magnetic Resonance, 40, 1-20.
887 Cheng, V.B., Suzukawa, H.H., and Wolfsberg, M. (1973) Investigations of a nonrandom numerical
888 method for multidimensional integration. The Journal of Chemical Physics, 59, 3992-3999.

Cho, H., and Rossman, G.R. (1993) Single-crystal NMR-studies of low-concentration hydrous species in minerals - grossular garnet. American Mineralogist, 78, 1149-1164.

Cohen-Addad, C., Ducros, P., Durif, A., Bertaut, E.F., and Delapalme, A. (1964) Détermination de la position des atomes d'hydrogène dans l'hydrogrinat Al_2O_3, 3CaO, $6H_2O$ par résonance magnétique nucléaire et diffraction neutronique. Journal de Physique, 25, 478-483.

Conroy, H. (1967) Molecular Schrödinger Equation. VIII. A New Method for the Evaluation of Multidimensional Integrals. The Journal of Chemical Physics, 47, 5307-5318.

Costa, F., and Chakraborty, S. (2008) The effect of water on Si and O diffusion rates in olivine and implications for transport properties and processes in the upper mantle. Physics of the Earth and Planetary Interiors, 166, 11-29.

Crepisson, C., Bureau, H., Blanchard, M., Ingrin, J., and Balan, E. (2014) Theoretical infrared spectrum of partially protonated cationic vacancies in forsterite. European Journal of Mineralogy, 26, 203-210.

Dai, L., and Karato, S. (2014a) High and highly anisotropic electrical conductivity of the asthenosphere due to hydrogen diffusion in olivine. Earth and Planetary Science Letters, 408, 79-86.

--- (2014b) The effect of pressure on the electrical conductivity of olivine under the hydrogen-rich conditions. Physics of the Earth and Planetary Interiors, 232, 51-56.

Dal Corso, A. (2014) Pseudopotentials periodic table: From H to Pu. Computational Materials Science, 95, 337-350.

Demouchy, S., and Mackwell, S. (2003) Water diffusion in synthetic iron-free forsterite. Physics and Chemistry of Minerals, 30, 486-494.

Du Frane, W.L., and Tyburczy, J.A. (2012) Deuterium-hydrogen exchange in olivine: Implications for point defects and electrical conductivity. Geochemistry, Geophysics, Geosystems, 13, Q03004.

Fei, H., Wiedenbeck, M., Yamazaki, D., and Katsura, T. (2013) Small effect of water on upper-mantle

913 rheology based on silicon self-diffusion coefficients. Nature, 498, 213-215.
914 Ferot, A., and Bolfan-Casanova, N. (2012) Water storage capacity in olivine and pyroxene to 14 GPa:
915 Implications for the water content of the Earth's upper mantle and nature of seismic
916 discontinuities. Earth and Planetary Science Letters, 349, 218-230.
917 Finger, L.W., Hazen, R.M., and Prewitt, C.T. (1991) Crystal structures of $Mg_{12}Si_4O_{19}(OH)_2$ (phase B)
918 and $Mg_{14}Si_5O_{24}$ (phase AnhB). American Mineralogist, 76, 1-7.
919 Gaetani, G.A., O'Leary, J.A., Koga, K.T., Hauri, E.H., Rose-Koga, E.F., and Monteleone, B.D. (2014)
920 Hydration of mantle olivine under variable water and oxygen fugacity conditions. Contributions
921 to Mineralogy and Petrology, 167, 965.
922 Giannozzi, P., Baroni, S., Bonini, N., Calandra, M., Car, R., Cavazzoni, C., Ceresoli, D., Chiarotti, G.L.,
923 Cococcioni, M., Dabo, I., and others. (2009) QUANTUM ESPRESSO: a modular and
924 open-source software project for quantum simulations of materials. Journal of Physics:
925 Condensed Matter, 21, 395502.
926 Grant, K.J., Kohn, S.C., and Brooker, R.A. (2006) Solubility and partitioning of water in synthetic
927 forsterite and enstatite in the system $MgO–SiO_2–H_2O±Al_2O_3$. Contributions to Mineralogy and
928 Petrology, 151, 651-664.
929 Griffin, J.M., and Ashbrook, S.E. (2013) Chapter Five - Solid-State NMR of High-Pressure Silicates in
930 the Earth’s Mantle. In A.W. Graham, Ed. Annual Reports on NMR Spectroscopy, Volume 79, p.
931 241-332. Academic Press.
932 Griffin, J.M., Berry, A.J., Frost, D.J., Wimperis, S., and Ashbrook, S.E. (2013) Water in the Earth's
933 mantle: a solid-state NMR study of hydrous wadsleyite. Chemical Science, 4, 1523-1538.
934 Haiber, M., Ballone, P., and Parrinello, M. (1997) Structure and dynamics of protonated Mg_2SiO_4: An
935 ab-initio molecular dynamics study. American Mineralogist, 82, 913-922.
936 Hazen, R.M., Downs, R.T., Finger, L.W., and Ko, J. (1993) Crystal chemistry of ferromagnesian silicate

spinels: Evidence for Mg-Si disorder. American Mineralogist, 78, 1320-1323.

Hirth, G., and Kohlstedt, D.L. (2003) Rheology of the upper mantle and the mantle wedge: a view from the experimentalists. In J. Eiler, Ed. Inside the Subduction Factory. Geophysical Monograph Series, 138, p. 83-105. American Geophysical Union, Washington, D.C.

Hohwy, M., Bildsøe, H., Jakobsen, H.J., and Nielsen, N.C. (1999) Efficient Spectral Simulations in NMR of Rotating Solids. The γ-COMPUTE Algorithm. Journal of Magnetic Resonance, 136, 6-14.

Horiuchi, H., and Sawamoto, H. (1981) ß-Mg_2SiO_4: Single-crystal X-ray diffraction study. American Mineralogist, 66, 568-575.

Horiuchi, H., Morimoto, N., Yamamoto, K., and Akimoto, S. (1979) Crystal structure of $2Mg_2SiO_4.3Mg(OH)_2$, a new high-pressure structure type. American Mineralogist, 64, 593-598.

Hugh-Jones, D.A., and Angel, R.J. (1994) A compressional study of $MgSiO_3$ orthoenstatite up to 8.5 GPa. American Mineralogist, 79, 405-410.

Hushur, A., Manghnani, M.H., Smyth, J.R., Nestola, F., and Frost, D.J. (2009) Crystal chemistry of hydrous forsterite and its vibrational properties up to 41 GPa. American Mineralogist, 94, 751-760.

Ingrin, J., Liu, J., Depecker, C., Kohn, S.C., Balan, E., and Grant, K.J. (2013) Low-temperature evolution of OH bands in synthetic forsterite, implication for the nature of H defects at high pressure. Physics and Chemistry of Minerals, 40, 499-510.

Kagi, H., Parise, J.B., Cho, H., and Rossman, G.R. (2000) Hydrogen bonding interactions in phase A $[Mg_7Si_2O_8(OH)_6]$ at ambient and high pressure. Physics and Chemistry of Minerals, 27, 225-233.

Kanzaki, M. (2010) Crystal structure of a new high-pressure polymorph of topaz-OH. American Mineralogist, 95, 1349-1352.

Kanzaki, M., and Xue, X. (2012) Structural characterization of moganite-type $AlPO_4$ by NMR and powder X-ray diffraction. Inorganic Chemistry, 51, 6164-6172.

961 --- (2016) Cation distribution in Mg-Zn olivine solid solution: a ^{29}Si MAS NMR and first-principles
962 calculation study. Journal of Mineralogical and Petrological Sciences, 111, 292-296.
963 Kanzaki, M., Stebbins, J.F., and Xue, X. (1992) Characterization of crystalline and amorphous silicates
964 quenched from high pressure by ^{29}Si MAS NMR spectroscopy. In Y. Syono, and M.H. Manghnani,
965 Eds. High-Pressure Research: Application to Earth and Planetary Sciences, 67, p. 89-100. Terra
966 Scientific Publishing Company, Tokyo.
967 Karato, S. (1990) The role of hydrogen in the electrical conductivity of the upper mantle. Nature, 347,
968 272-273.
969 --- (2013) Theory of isotope diffusion in a material with multiple species and its implications for
970 hydrogen-enhanced electrical conductivity in olivine. Physics of the Earth and Planetary Interiors,
971 219, 49-54.
972 --- (2015) Some notes on hydrogen-related point defects and their role in the isotope exchange and
973 electrical conductivity in olivine. Physics of the Earth and Planetary Interiors, 248, 94-98.
974 Keppler, H., and Rauch, M. (2000) Water solubility in nominally anhydrous minerals measured by FTIR
975 and ^{1}H MAS NMR: the effect of sample preparation. Physics and Chemistry of Minerals, 27,
976 371-376.
977 Keppler, H., and Smyth, J.R., Eds. (2006) Water in Nominally Anhydrous Minerals, 62, 478 p. Reviews
978 in Mineralogy and Geochemistry, Mineralogical Society of America, Chantilly, Virginia.
979 Koch-Muller, M., Dera, P., Fei, Y., Hellwig, H., Liu, Z., Van Orman, J., and Wirth, R. (2005)
980 Polymorphic phase transition in Superhydrous Phase B. Physics and Chemistry of Minerals, 32,
981 349-361.
982 Koch-Muller, M., Matsyuk, S.S., Rhede, D., Wirth, R., and Khisina, N. (2006) Hydroxyl in mantle
983 olivine xenocrysts from the Udachnaya kimberlite pipe. Physics and Chemistry of Minerals, 33,
984 276-287.

Kohlstedt, D.L., Keppler, H., and Rubie, D.C. (1996) Solubility of water in the α, β and γ phases of $(Mg,Fe)_2SiO_4$. Physics and Chemistry of Minerals, 123, 345-357.

Kohn, S.C. (1996) Solubility of H_2O in nominally anhydrous mantle minerals using ^1H MAS NMR. American Mineralogist, 81, 1523-1526.

--- (2006) Structural studies of OH in nominally anhydrous minerals using NMR. Reviews in Mineralogy and Geochemistry, 62, 53-66.

Kovacs, I., O'Neill, H.S.C., Hermann, J., and Hauri, E.H. (2010) Site-specific infrared O-H absorption coefficients for water substitution into olivine. American Mineralogist, 95, 292-299.

Kovacs, I., Green, D.H., Rosenthal, A., Hermann, J., O'Neill, H.S., Hibberson, W.O., and Udvardi, B. (2012) An Experimental Study of Water in Nominally Anhydrous Minerals in the Upper Mantle near the Water-saturated Solidus. Journal of Petrology, 53, 2067-2093.

Kudoh, Y., Kuribayashi, T., Kagi, H., and Inoue, T. (2006) Cation vacancy and possible hydrogen positions in hydrous forsterite, $Mg_{1.985}Si_{0.993}H_{0.06}O_4$, synthesized at 13.5 GPa and 1300 °C. Journal of Mineralogical and Petrological Sciences, 101, 265-269.

Lager, G.A., Armbruster, T., and Faber, J. (1987) Neutron and X-ray diffraction study of hydrogarnet $Ca_3Al_2(O_4H_4)_3$. American Mineralogist, 72, 756-765.

Lager, G.A., Armbruster, T., Rotella, F.J., and Rossman, G.R. (1989) OH substitution in garnets: X-ray and neutron diffraction, infrared, and geometric-modeling studies. American Mineralogist, 74, 840-851.

Lemaire, C., Kohn, S.C., and Brooker, R.A. (2004) The effect of silica activity on the incorporation mechanisms of water in synthetic forsterite: a polarised infrared spectroscopic study. Contributions to Mineralogy and Petrology, 147, 48-57.

Libowitzky, E. (1999) Correlation of O-H stretching frequencies and O-H···O hydrogen bond lengths in minerals. Monatshefte fur Chemie, 130, 1047-1059.

Libowitzky, E., and Beran, A. (1995) OH defects in forsterite. Physics and Chemistry of Minerals, 22, 387-392.

Litasov, K.D., Ohtani, E., Kagi, H., Jacobsen, S.D., and Ghosh, S. (2007) Temperature dependence and mechanism of hydrogen incorporation in olivine at 12.5-14.0 GPa. Geophysical Research Letters, 34, L16314.

Malfait, W.J., and Xue, X. (2010) The nature of hydroxyl groups in aluminosilicate glasses: quantifying Si-OH and Al-OH abundances along the SiO_2-$NaAlSiO_4$ join by ^{1}H, ^{27}Al-^{1}H and ^{29}Si-^{1}H NMR spectroscopy. Geochimica et Cosmochimica Acta, 74, 719-737.

Manghnani, M.H., Hushur, A., Smyth, J.R., Nestola, F., Dera, P., Sekar, M., Amulele, G., and Frost, D.J. (2013) Compressibility and structural stability of two variably hydrated olivine samples ($Fo_{97}Fa_3$) to 34 GPa by X-ray diffraction and Raman spectroscopy. American Mineralogist, 98, 1972-1979.

Maricq, M.M., and Waugh, J.S. (1979) NMR in rotating solids. Journal of Chemical Physics, 70, 3300-3316.

Matsyuk, S.S., and Langer, K. (2004) Hydroxyl in olivines from mantle xenoliths in kimberlites of the Siberian platform. Contributions to Mineralogy and Petrology, 147, 413-437.

Matveev, S., O'Neill, H.S., Ballhaus, C., Taylor, W.R., and Green, D.H. (2001) Effect of silica activity on OH^- IR spectra of olivine: Implications for low-$aSiO_2$ mantle metasomatism. Journal of Petrology, 42, 721-729.

Miller, G.H., Rossman, G.R., and Harlow, G.E. (1987) The natural occurrence of hydroxide in olivine. Physics and Chemistry of Minerals, 14, 461-472.

Momma, K., and Izumi, F. (2011) VESTA 3 for three-dimensional visualization of crystal, volumetric and morphology data. Journal of Applied Crystallography, 44, 1272‑1276.

Mosenfelder, J.L., Deligne, N.I., Asimow, P.D., and Rossman, G.R. (2006) Hydrogen incorporation in olivine from 2-12 GPa. American Mineralogist, 91, 285-294.

Ohashi, Y. (1984) Polysynthetically-twinned structures of enstatite and wollastonite. Physics and Chemistry of Minerals, 10, 217-229.

Otsuka, K., and Karato, S. (2011) Control of the water fugacity at high pressures and temperatures: Applications to the incorporation mechanisms of water in olivine. Physics of the Earth and Planetary Interiors, 189, 27-33.

Padrón-Navarta, J.A., Hermann, J., and O'Neill, H.S.C. (2014) Site-specific hydrogen diffusion rates in forsterite. Earth and Planetary Science Letters, 392, 100-112.

Perdew, J.P., Burke, K., and Ernzerhof, M. (1996) Generalized gradient approximation made simple. Physical Review Letters, 77, 3865-3868.

Perdew, J.P., Ruzsinszky, A., Csonka, G.I., Vydrov, O.A., Scuseria, G.E., Constantin, L.A., Zhou, X., and Burke, K. (2008) Restoring the Density-Gradient Expansion for Exchange in Solids and Surfaces. Physical Review Letters, 100, 136406.

Phillips, B.L., Burnley, P.C., Worminghaus, K., and Navrotsky, A. (1997) ^{29}Si and ^{1}H NMR spectroscopy of high-pressure hydrous magnesium silicates. Physics and Chemistry of Minerals, 24, 179-190.

Pickard, C.J., and Mauri, F. (2001) All-electron magnetic response with pseudopotentials: NMR chemical shifts. Physical Review B, 63, 245101.

Piriou, B., and McMillan, P. (1983) The high-frequency vibrational spectra of vitreous and crystalline orthosilicates. American Mineralogist, 68, 426-443.

Poe, B.T., Romano, C., Nestola, F., and Smyth, J.R. (2010) Electrical conductivity anisotropy of dry and hydrous olivine at 8 GPa. Physics of the Earth and Planetary Interiors, 181, 103-111.

Shaw, D.M., and Tse, J.S. (2007) Vibrational dynamics in H^{+}-substituted forsterite: A first-principles molecular dynamics study. American Mineralogist, 92, 1593-1600.

Smyth, J.R., Frost, D.J., Nestola, F., Holl, C.M., and Bromiley, G. (2006) Olivine hydration in the deep upper mantle: Effects of temperature and silica activity. Geophysical Research Letters, 33,

L15301.

Stebbins, J.F. (1995) Nuclear magnetic resonance spectroscopy of silicates and oxides in geochemistry and geophysics. In T.J. Ahrens, Ed. Mineral Physics & Crystallography, A Handbook of Physical Constants, p. 303-331. American Geophysical Union, Washington, DC.

Stebbins, J.F., and Xue, X. (2014) NMR Spectroscopy of Inorganic Earth Materials. Reviews in Mineralogy and Geochemistry, 78, 605-653.

Stebbins, J.F., Panero, W.R., Smyth, J.R., and Frost, D.J. (2009) Forsterite, wadsleyite, and ringwoodite (Mg_2SiO_4): ^{29}Si NMR constraints on structural disorder and effects of paramagnetic impurity ions. American Mineralogist, 94, 626-629.

Umemoto, K., Wentzcovitch, R.M., Hirschmann, M.M., Kohlstedt, D.L., and Withers, A.C. (2011) A first-principles investigation of hydrous defects and IR frequencies in forsterite: The case for Si vacancies. American Mineralogist, 96, 1475-1479.

Verma, A.K., and Karki, B.B. (2009) Ab initio investigations of native and protonic point defects in Mg_2SiO_4 polymorphs under high pressure. Earth and Planetary Science Letters, 285, 140-149.

Vinogradov, E., Madhu, P.K., and Vega, S. (1999) High-resolution proton solid-state NMR spectroscopy by phase-modulated Lee-Goldburg experiment. Chemical Physics Letters, 314, 443-450.

Walker, A.M., Wright, K., and Slater, B. (2003) A computational study of oxygen diffusion in olivine. Physics and Chemistry of Minerals, 30, 536-545.

Walker, A.M., Demouchy, S., and Wright, K. (2006) Computer modelling of the energies and vibrational properties of hydroxyl groups in α- and β-Mg_2SO_4. European Journal of Mineralogy, 18, 529-543.

Walker, A.M., Hermann, J., Berry, A.J., and O'Neill, H.S.C. (2007) Three water sites in upper mantle olivine and the role of titanium in the water weakening mechanism. Journal of Geophysical Research-Solid Earth, 112, B05211.

Wang, D., Mookherjee, M., Xu, Y., and Karato, S. (2006) The effect of water on the electrical conductivity of olivine. Nature, 443, 977-980.

Withers, A.C., Hirschmann, M.M., and Tenner, T.J. (2011) The effect of Fe on olivine H_2O storage capacity: Consequences for H_2O in the martian mantle. American Mineralogist, 96, 1039-1053.

Wright, K., and Catlow, C.R.A. (1994) A computer simulation study of (OH) defects in olivine. Physics and Chemistry of Minerals, 20, 515-518.

Wu, G., and Wasylishen, R.E. (1993) NMR lineshapes arising from a pair of nonequivalent homonuclear spins in magic-angle-spinning experiments. Journal of Magnetic Resonance A, 102, 183-189.

Xue, X., and Kanzaki, M. (2004) Dissolution mechanisms of water in depolymerized silicate melts: Constraints from ^{1}H and ^{29}Si NMR spectroscopy and ab initio calculations. Geochimica et Cosmochimica Acta, 68, 5027-5057.

--- (2007a) Al coordination and water speciation in hydrous aluminosilicate glasses: direct evidence from high-resolution heteronuclear ^{1}H - ^{27}Al correlation NMR. Solid State Nuclear Magnetic Resonance, 31, 10-27.

--- (2007b) High-pressure δ-$Al(OH)_3$ and δ-AlOOH phases and isostructural hydroxides/oxyhydroxides: New structural insights from high-resolution ^{1}H and ^{27}Al NMR. Journal of Physical Chemistry B, 111, 13156-13166.

--- (2009) Proton distributions and hydrogen bonding in crystalline and glassy hydrous silicates and related inorganic materials: insights from high-resolution solid-state NMR spectroscopy. Journal of the American Ceramic Society, 92, 2803-2830.

Xue, X., Kanzaki, M., and Fraser, D.G. (2002) The dissolution mechanisms of forsterite and enstatite: Constraints from ^{29}Si and ^{1}H MAS NMR. Geochimica et Cosmochimica Acta, 66, A853.

Xue, X., Kanzaki, M., Fukui, H., Ito, E., and Hashimoto, T. (2006) Cation order and hydrogen bonding of high-pressure phases in the Al_2O_3-SiO_2-H_2O system: An NMR and Raman study. American

Mineralogist, 91, 850-861.

Xue, X., Kanzaki, M., and Shatskiy, A. (2008) Dense hydrous magnesium silicates, phase D and superhydrous B: New structural constraints from one- and two- dimensional ^{29}Si and ^{1}H NMR. American Mineralogist, 93, 1099-1111.

Xue, X., Kanzaki, M., and Fukui, H. (2010) Unique crystal chemistry of two polymorphs of topaz-OH: a multi-nuclear NMR and Raman study. American Mineralogist, 95, 1276-1293.

Yang, H., and Ghose, S. (1995) High temperature single crystal X-ray diffraction studies of the ortho-proto phase transition in enstatite, $Mg_2Si_2O_6$ at 1360 K. Physics and Chemistry of Minerals, 22, 300-310.

Yang, X.Z. (2016) Effect of oxygen fugacity on OH dissolution in olivine under peridotite-saturated conditions: An experimental study at 1.5-7 GPa and 1100-1300 °C. Geochimica Et Cosmochimica Acta, 173, 319-336.

Yesinowski, J.P., Eckert, H., and Rossman, G.R. (1988) Characterization of hydrous species in minerals by high-speed ^{1}H MAS-NMR. Journal of American Chemical Society, 110, 1367-1375.

Yoshino, T., Matsuzaki, T., Shatskiy, A., and Katsura, T. (2009) The effect of water on the electrical conductivity of olivine aggregates and its implications for the electrical structure of the upper mantle. Earth and Planetary Science Letters, 288, 291-300.

Zaremba, S.K. (1966) Good lattice points, discrepancy, and numerical integration. Annali di Matematica Pura ed Applicata, 73, 293-317.

Zigan, F., and Rothbauer, R. (1967) Neutronenbeugungsmessungen am brucit. Zeitschrift fur Kristallographie, 167, 137-143.

Figure captions

Figure 1. Typical unpolarized Raman spectrum in the O-H stretching region for a forsterite sample containing about 0.5 wt% H_2O.

Figure 2. ^1H static and MAS NMR spectra (at a spinning rate of 10, 20 and 30 kHz from top to bottom as marked) obtained with a recycle delay time of 60 s (**a**), and expanded view around the central band for the MAS spectra (at a spinning rate of 10, 20 and 30 kHz from top to bottom as marked) (**b**) for a forsterite sample containing about 0.5 wt% H_2O. All spectra have been processed with a Gaussian line broadening function of 20 Hz, and plotted with the same maximum peak height.

Figure 3. Expanded view around the central band of the ^1H MAS NMR spectra obtained at a spinning rate of 20 kHz with a recycle delay time (d1) of 60 s (**top**) and 3 s (**middle**), and the difference spectrum of the two (**bottom**), for a forsterite sample containing about 0.5 wt% H_2O. All spectra are plotted with a common intensity scale. The red dashed line is a guide for the small component near 5 ppm that has a shorter ^1H T_1 and is absent in the difference spectrum.

Figure 4. 2D rotor-synchronized ^1H NOESY spectra obtained at a spinning rate of 20 kHz with a recycle delay of 15 s and a mixing time of 2 μs (**a**) and 200 ms (**b**) for a forsterite sample containing about 0.5 wt% H_2O. A Gaussian line broadening of 100 Hz has been applied to both dimensions. The contours are plotted in a nonlinear intensity scale with a minimum relative intensity of 0.05 (of the maximum) and a scale factor of 1.5. The dotted diagonal line is a guide for positions of diagonal peaks. Also plotted to the right are F2 cross sections at F1 positions of about 7.3 ppm, 1.1 ppm and -3 ppm (bottom to top) with a common vertical scale for the former two and an expanded vertical scale (5×) for the latter.

Figure 5. 2D rotor-synchronized ^1H CRAMPS (FSLG) - MAS NMR spectra obtained at a spinning rate of 25 kHz with a recycle delay of 15 s and a mixing time of 2 μs (**a**) and 200 ms (**b**) for a forsterite sample containing about 0.5 wt% H_2O. A Gaussian line broadening of 100 Hz and 20 Hz have been applied to the F2 and F1 dimensions,

respectively. The contours are plotted in a nonlinear intensity scale with a minimum relative intensity of 0.05 (of the maximum) and a scale factor of 1.5. The dotted diagonal line is a guide for positions of diagonal peaks. Also plotted to the right are F1 cross sections at F2 positions of about 7.3 ppm, 1.5 ppm and -2 ppm (bottom to top) with an expanded vertical scale (5×) for the upper and bottom cross sections (relative to the middle one).

Figure 6. ^{29}Si MAS NMR spectrum obtained at a spinning rate of 20 kHz for a forsterite sample containing about 0.5 wt% H_2O. A Gaussian line broadening of 5 Hz has been applied. Fo: forsterite; CEn: low-pressure clinoenstatite.

Figure 7. ^{29}Si MAS NMR spectrum (**top**) and ^{1}H-^{29}Si CP-MAS NMR spectra obtained at a contact time of 2, 4, 8 and 20 ms (**bottom to top as labelled**) for a hydrous forsterite sample containing about 0.5 wt% H_2O. The spinning rate was 20 kHz for all. The four CP spectra are plotted with a common intensity scale for comparison. A Gaussian line broadening of 5 Hz has been applied to all spectra.

Figure 8. Simulation result for ^{1}H-^{29}Si CP-MAS NMR spectra obtained at a contact time of 2, 4, 8 and 20 ms (**bottom to top as labelled**) as shown in Figure 7, with three mixed Gaussian-Lorentzian components. The black dotted, red solid and blue solid curves represent the experimental spectra, simulated spectra and simulated components, respectively. Al the spectra are plotted with a common intensity scale for comparison. A Gaussian line broadening of 5 Hz has been applied to the experimental spectra.

Figure 9. Crystal structure of representative lowest-energy forsterite 2 × 1 × 2 supercell models with four H ions associated with a vacant tetrahedral Si site ($(4H)_{Si}$ model 1) (**a**), and two H ions associated with a vacant octahedral M1 site, each bonded to a SiO_4 tetrahedron and forming a hydrogen bond with an oxygen on an adjacent SiO_4 tetrahedron ($(2H)_{M1}$ model 1) (**b**). Blue tetrahedra and orange octahedra stand for SiO_4 tetrahedra and MgO_6 octahedra, respectively. Red and white spheres stand for oxygen and hydrogen atoms. Thin black box delineates the supercell dimension. Drawn using the Vesta program (Momma and Izumi 2011).

Figure 10. Configuration of the four hydrogen ions associated with a vacant tetrahedral site for the six studied $(4H)_{Si}$ models as labelled. Drawn using the Vesta program (Momma and Izumi 2011).

Figure 11. Structure of the $(4H)_{Si}$ model 5 with three adjacent interstitual octahedral sites I2 (outlined in grey

1176 octahedra) each occupied by a hydrogen ion. Others as Figures 9-10. The I2 interstitual sites alternate with M2 sites
1177 along *c* direction. The vacant tetrahedron is below the paper with O1 apex pointing into the paper. The other apexes
1178 at the base of the vacant tetrahedra (O2, O3, O3') and the H atoms bonded to each (H4, H1, H3) are labelled. Note
1179 that for $(4H)_{Si}$ models 1 to 4, one or two of the three I2 interstitual octahedral sites would each accommodate a
1180 hydrogen ion. Drawn using the Vesta program (Momma and Izumi 2011).

1181 **Figure 12**. Comparison of experimental ^{1}H static NMR spectrum for hydrous forsterite as in Figure 2, with simulated
1182 ^{1}H static NMR powder spectra for the two lowest-energy $(4H)_{Si}$ models 1 and 2, and the $(2H)_{M1}$ model 1, as
1183 labelled, using the SIMPSON program (Bak et al. 2000).

1184 **Figure 13**. Comparison of experimental ^{1}H MAS NMR spectrum for hydrous forsterite as in Figure 2, with simulated
1185 ^{1}H MAS NMR powder spectra for the two lowest-energy $(4H)_{Si}$ models 1 and 2, and the $(2H)_{M1}$ model 1, as
1186 labelled, using the SIMPSON program (Bak et al. 2000), all at a spinning rate of 20 kHz.

Table 1. Comparison of calculated unit cell volumes (V) and ^{29}Si and ^{1}H NMR parameters at 0 GPa with experimental data under ambient condition for selected Mg silicate minerals

Phase	Formula	V, calc (Å^3)	V, exp (Å^3)	H site	σ_i^H, calc (ppm)	δ_i^H, calc (ppm)	δ_i^H, exp (ppm)	Si site	σ_i^{Si}, calc (ppm)	δ_i^{Si}, calc (ppm)	δ_i^{Si}, exp (ppm)	Ref, structure[a]	Ref, NMR[a]
forsterite	Mg_2SiO_4	290.85	290.107(17)						408.15	-61.80	-61.8	[1]	[11],[12]
wadsleyite	Mg_2SiO_4	541.55	538.14						426.52	-80.17	-78.7	[2]	[11]
ringwoodite	Mg_2SiO_4	527.62	525.73(4)						428.56	-82.21	-81.3	[3]	[11]
protoenstatite	$MgSiO_3$	431.82							432.65	-86.30	-84.9	[4]	[13]
clinoenstatite	$MgSiO_3$	417.00	415.5(2)					Si1	431.77	-85.42	-83.3	[5]	[14]
								Si2	427.73	-81.38	-80.5		
orthoenstatite	$MgSiO_3$	835.26	833.0(1)					Si1	431.54	-85.19	-83.2	[6]	[15],[16]
								Si2	427.88	-81.53	-80.7		
brucite	$Mg(OH)_2$	39.23	40.75		29.31	0.00	0.0					[7]	[17]
phase A	$Mg_7Si_2O_8(OH)_6$	508.59	511.23(2)	H1	25.96	3.35	3.6	Si1	414.61	-68.26	-70.6	[8]	[14],[17]
				H2	27.16	2.15	2.2	Si2	410.34	-63.99	-63.9		
phase B	$Mg_{12}Si_4O_{19}(OH)_2$	1469.79	1458.4(3)	H1	26.33	2.98	3.3	Si1	513.34	-166.99	-170.4	[9]	[18]
				H2	25.82	3.49	4.7	Si2	411.77	-65.42	-64		
								Si3	421.40	-75.05	-75.8		
								Si4	420.65	-74.30	-75		
superhydrous B	$Mg_{10}Si_3O_{14}(OH)_4$	625.12	625.71	H1	25.85	3.46	3.82	Si1	508.96	-162.61	-166.6	[10]	[19]
				H2	25.82	3.49	3.92	Si2	420.09	-73.74	-74.5		

[a] [1] Smyth et al. (2006); [2] Horiuchi and Sawamoto (1981); [3] Hazen et al. (1993); [4] Yang and Ghose (1995); [5] Ohashi (1984); [6] Hugh-Jones and Angel (1994); [7] Zigan and Rothbauer (1967); [8] Kagi et al. (2000) ; [9] Finger et al. (1991); [10] Koch-Muller et al. (2005); [11] Stebbins et al. (2009); [12] This study; [13] Xue et al. (2002); [14] Kanzaki et al. (1992); [15]Ashbrook et al. (2007b); [16] Xue and Kanzaki (unpublished data); [17] Xue and Kanzaki (2009); [18] Phillips et al. (1997); [19] Xue et al. (2008).

1187

1188

This is a preprint, the final version is subject to change, of the American Mineralogist (MSA)
Cite as Authors (Year) Title. American Mineralogist, in press.
(DOI will not work until issue is live.) DOI: http://dx.doi.org/10.2138/am-2017-5878

Table 2. ^{1}H and ^{29}Si NMR parameters of hydrous forsterite

^{1}H Peak	δ_i^H (ppm)	^{1}H FWHM[a] (ppm)	^{29}Si Peak	δ_i^{Si} (ppm)	^{29}Si FWHM (ppm)
1	1.2	1.15	MAS	-61.7	0.18
2	2.4	8.7	CP, peak 1	-60.9	0.17
3	7.3	0.14	CP, peak 2	-61.7	0.42
			CP, peak 3	-62.1	0.45

[a] FWHM at 30 kHz MAS.

1189

1190

This is a preprint, the final version is subject to change, of the American Mineralogist (MSA)
Cite as Authors (Year) Title. American Mineralogist, in press.
(DOI will not work until issue is live.) DOI: http://dx.doi.org/10.2138/am-2017-5878

Table 3. Enthalpies of forsterite 2×1×2 supercell models at 0 and 12 GPa from DFT calculation

	0 GPa				12 GPa					
Model	E (Ry)	ΔE (Ry)	ΔE (eV)	ΔE (kJ/mol)	V (Å^3)	E (Ry)	H (Ry)	ΔH (Ry)	ΔH (eV)	ΔH (kJ/mol)
forsterite[a]	-4426.1863				1073.78	-4425.9553	-4420.0436			
$(4H)_{Si}$ model 1	-4384.9299	0.0000	0.000	0.04	1075.20	-4384.6933	-4378.7738	0.0000	0.000	0.00
$(4H)_{Si}$ model 2	-4384.9299	0.0000	0.000	0.00	1075.63	-4384.6929	-4378.7710	0.0028	0.038	3.64
$(4H)_{Si}$ model 3	-4384.9235	0.0065	0.088	8.47	1076.45	-4384.6857	-4378.7593	0.0145	0.198	19.07
$(4H)_{Si}$ model 4	-4384.9128	0.0171	0.232	22.41	1076.70	-4384.6742	-4378.7465	0.0273	0.372	35.88
$(4H)_{Si}$ model 5	-4384.9023	0.0276	0.376	36.29	1078.40	-4384.6633	-4378.7262	0.0476	0.648	62.52
$(4H)_{Si}$ model 6	-4384.9148	0.0151	0.206	19.88	1075.29	-4384.6786	-4378.7587	0.0152	0.206	19.89
$(2H)_{M1}$ model 1	-4395.5279	0.0000	0.000	0.00	1070.71	-4395.2909	-4389.3962	0.0000	0.000	0.00
$(2H)_{M2}$ model 1	-4395.4797	0.0483	0.657	63.38	1071.98	-4395.2381	-4389.3364	0.0599	0.814	78.57

Note: E: internal energy; V: volume; H: enthalpy; ΔH (ΔE): enthalpy (energy) difference relative to the lowest-enthalpy model of a given stoichiometry at a given pressure. H = E + PV.

[a] Forsterite expressed in terms of 2×1×2 supercell for easy comparison.

1193

Table 4. Comparison of unit cell parameters of forsterite from DFT calculation at 0 GPa with experimental data under ambient condition

Model/sample	H_2O content (wt%)	a (Å)	b (Å)	c (Å)	α (°)	β (°)	γ (°)	V (Å^3)	Δa[a] (%)	Δb[a] (%)	Δc[a] (%)	ΔV[a] (%)	Ref[b]
DFT calculation:													
forsterite	0	4.7613	10.2037	5.9867	90.00	90.00	90.00	290.8524	0.000	0.000	0.000	0.000	[1]
$(4H)_{Si}$ model 1	1.618	4.7567	10.2261	5.9973	90.00	90.00	90.13	291.7238	-0.096	0.219	0.177	0.300	[1]
$(4H)_{Si}$ model 2	1.618	4.7536	10.2287	6.0030	90.06	89.90	90.02	291.8866	-0.161	0.245	0.271	0.356	[1]
$(4H)_{Si}$ model 3	1.618	4.7586	10.2309	6.0015	89.99	90.09	90.03	292.1802	-0.057	0.266	0.247	0.456	[1]
$(4H)_{Si}$ model 4	1.618	4.7595	10.2378	5.9984	90.00	90.00	90.04	292.2834	-0.038	0.334	0.195	0.492	[1]
$(4H)_{Si}$ model 5	1.618	4.7631	10.2435	6.0006	90.00	90.00	90.13	292.7723	0.038	0.390	0.231	0.660	[1]
$(4H)_{Si}$ model 6	1.618	4.7605	10.2252	5.9925	90.26	90.07	90.02	291.6941	-0.016	0.210	0.096	0.289	[1]
$(2H)_{M1}$ model 1	0.808	4.7705	10.2301	5.9558	90.32	90.16	90.22	290.6544	0.194	0.259	-0.516	-0.068	[1]
$(2H)_{M2}$ model 1	0.808	4.7573	10.1983	6.0094	90.13	90.03	89.60	291.5433	-0.085	-0.053	0.379	0.238	[1]
Experimental[c]:													
Fo, anhydrous	<0.001	4.75518(18)	10.19853(22)	5.98215(22)	90	90	90	290.107(17)	0.00	0.00	0.00	0.000	[2]
SZ0408A	0.89	4.75454(39)	10.20675(75)	5.98625(39)	90	90	90	290.503(31)	-0.013	0.081	0.069	0.136	[2]
SZ0408B	0.85	4.75465(39)	10.20416(75)	5.98494(39)	90	90	90	290.373(31)	-0.011	0.055	0.047	0.091	[2]
SZ0410B	0.45	4.75574(17)	10.20383(58)	5.98383(51)	90	90	90	290.376(27)	0.012	0.052	0.028	0.092	[2]
SZ0411A	0.577	4.75659(36)	10.20096(65)	5.98258(48)	90	90	90	290.286(29)	0.030	0.024	0.007	0.061	[2]
SZ0409B	0.556	4.75517(46)	10.20481(66)	5.98640(38)	90	90	90	290.494(32)	0.000	0.062	0.071	0.132	[2]
SZ0501A	0.44	4.75463(48)	10.19925(55)	5.98346(39)	90	90	90	290.165(33)	-0.012	0.007	0.022	0.017	[2]
SZ0501B	0.34	4.75554(42)	10.19955(115)	5.98350(43)	90	90	90	290.226(42)	0.008	0.010	0.023	0.040	[2]
H2296	0.10	4.7557(10)	10.1977(16)	5.9821(8)	90	90	90	290.115(94)	0.011	-0.008	-0.001	0.002	[2]
Fo,hydrous	0.38(4)	4.756(1)	10.208(3)	5.988(2)	90	90	90	290.7(2)	0.017	0.093	0.098	0.208	[3]

Notes: Cell parameters from DFT calculation refer to a single unit cell. All relative to space group *Pbnm*.

[a] Relative differences in cell constants and volume (%) with respect to H-free forsterite.

[b] [1] This study; [2] Smyth et al. (2006); [3] Kudoh et al. (2006).

[c] Hydrous forsterite samples by Smyth et al. (2006) synthesized at 12 GPa and 1100-1600°C; That of Kudoh et al. (2006) synthesized at 13.5 GPa and 1300°C.

1194

This is a preprint, the final version is subject to change, of the American Mineralogist (MSA)
Cite as Authors (Year) Title. American Mineralogist, in press.
(DOI will not work until issue is live.) DOI: http://dx.doi.org/10.2138/am-2017-5878

Table 5. ^{1}H isotropic chemical shifts (δ_i^H) of forsterite 2×1×2 supercell models from GIPAW calculations

Model	H site	δ_i^H (ppm)	Comment
$(4H)_{Si}$ model 1	H1	0.52	bonded to O3
	H2	0.06	bonded to O1
	H3	0.52	bonded to O3'
	H4[a]	-0.44	bonded to O2
$(4H)_{Si}$ model 2	H1[a]	2.12	bonded to O3
	H2	1.41	bonded to O1
	H3	0.88	bonded to O3'
	H4	0.61	bonded to O2
$(4H)_{Si}$ model 3	H1	1.03	bonded to O3
	H2	0.39	bonded to O1
	H3[a]	1.80	bonded to O3'
	H4[a]	-0.75	bonded to O2
$(4H)_{Si}$ model 4	H1[a]	0.71	bonded to O3
	H2	0.00	bonded to O1
	H3[a]	0.71	bonded to O3'
	H4	0.36	bonded to O2
$(4H)_{Si}$ model 5	H1[a]	0.67	bonded to O3
	H2	0.30	bonded to O1
	H3[a]	0.67	bonded to O3'
	H4[a]	-1.02	bonded to O2
$(4H)_{Si}$ model 6	H1	-1.03	bonded to O3
	H2	1.68	bonded to O1
	H3	1.05	bonded to O3'
	H4	1.09	bonded to O2
$(2H)_{M1}$ model 1	H1, H2	7.67	bonded to O2
$(2H)_{M2}$ model 1	H1	7.41	bonded to O3
	H2	5.86	bonded to O3

[a] H pointing away from tetrahedral center.

1197

Table 6. ^{29}Si isotropic chemical shifts (δ_i^{Si}) of forsterite 2×1×2 supercell models from GIPAW calculations

Model	Si site	δ_i^{Si} (ppm)	$\Delta\delta_i^{Si}$ (ppm)[a]	R(Si-H) (Å)[b]	Comment[c]
forsterite		-61.80	0.00		
$(4H)_{Si}$ model 1	Si13	-61.54	0.26	2.562	close to H4-O2
	Others	-62.4 ~ -61.3	-0.6 ~ 0.5 (av. 0.0)		
$(4H)_{Si}$ model 2	Si11	-60.17	1.63	2.348	close to H1-O3
	Others	-62.1 ~ -61.6	-0.3 ~ 0.2 (av.0.1)		
$(4H)_{Si}$ model 3	Si10	-60.07	1.73	2.365	close to H3-O3
	Si13	-61.51	0.29	2.539	close to H4-O2
	Others	-62.7 ~ -61.2	-0.9 ~ 0.6 (av. 0.0)		
$(4H)_{Si}$ model 4	Si10	-60.27	1.53	2.373	close to H3-O3
	Si11	-60.27	1.53	2.373	close to H1-O3
	Others	-62.2 ~ -61.3	-0.4 ~ 0.5 (av.0.0)		
$(4H)_{Si}$ model 5	Si10	-60.13	1.67	2.364	close to H3-O3
	Si11	-60.13	1.67	2.364	close to H1-O3
	Si13	-61.46	0.34	2.514	close to H4-O2
	Others	-62.8 ~ -61.0	-1.0 ~ 0.8 (av. 0.0)		
$(4H)_{Si}$ model 6	All Si	-62.4 ~ -61.3	-0.6 ~ 0.5 (av. 0.0)		
$(2H)_{M1}$ model 1	Si1	-65.49	-3.69	2.272	Si-O2-H & -O3-V_{M1} (edge-share)
	Si3	-60.22	1.58	2.572	Si-O1-V_{M1}(corner-share)
	Si6	-60.22	1.58	2.572	Si-O1-V_{M1}(corner-share)
	Si8	-65.49	-3.69	2.272	Si-O2-H & -O3-V_{M1} (edge-share)
	Others	-61.9 ~ -61.4	-0.1 ~ 0.4 (av. 0.1)		
$(2H)_{M2}$ model 1	Si1	-63.59	-1.79	3.341	Si-O1-V_{M2}(corner-share)
	Si3	-66.75	-4.95	2.359	Si-O3-H & -O3-V_{M2} (edge-share)
	Si9	-62.47	-0.67	2.299	Si-O3-H (corner-share)
	Si10	-59.38	2.42	2.681	Si-O3-V_{M2}(corner-share)
	Si15	-60.53	1.27	3.340	Si-O2-V_{M2}(corner-share)
	Others	-62.0 ~ -61.4	-0.2 ~ 0.4 (av. 0.1)		

[a] Isotropic chemical shift difference from H-free forsterite. Numbers in brackets are the average values.
[b] Si-H distance. For $(4H)_{Si}$ models, only R(Si-H) < 3 Å are shown, whereas for $(2H)_M$ models, the shortest R(Si-H) for all Si sites adjacent to the vacant M site are shown.
[c] V_{M1} and V_{M2} stand for vacant M1 and M2 octahedron, respectively.

1198

1199

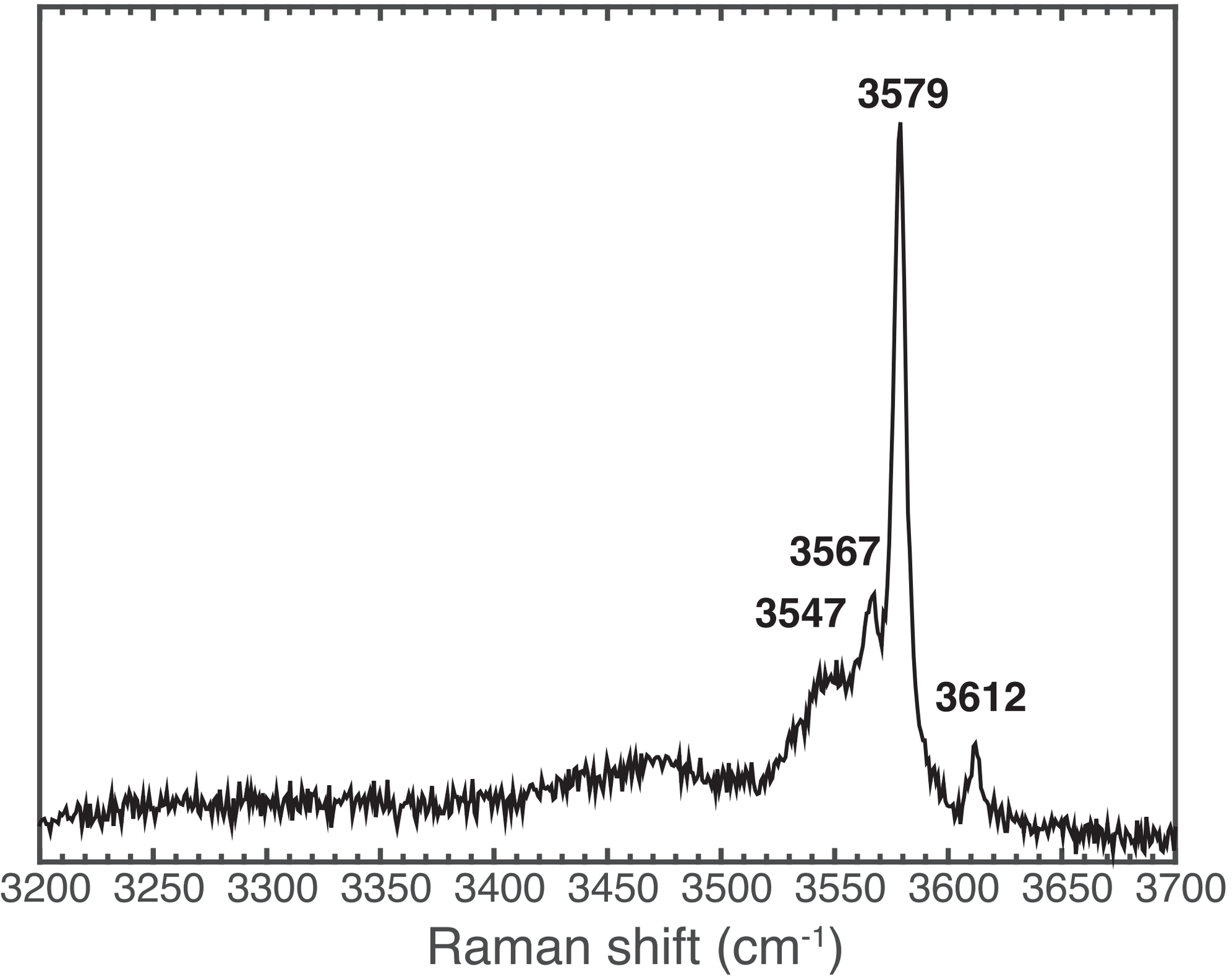
3579
3567
3547
3612
3200 3250 3300 3350 3400 3450 3500 3550 3600 3650 3700
Raman shift (cm-1)

Fig. 1

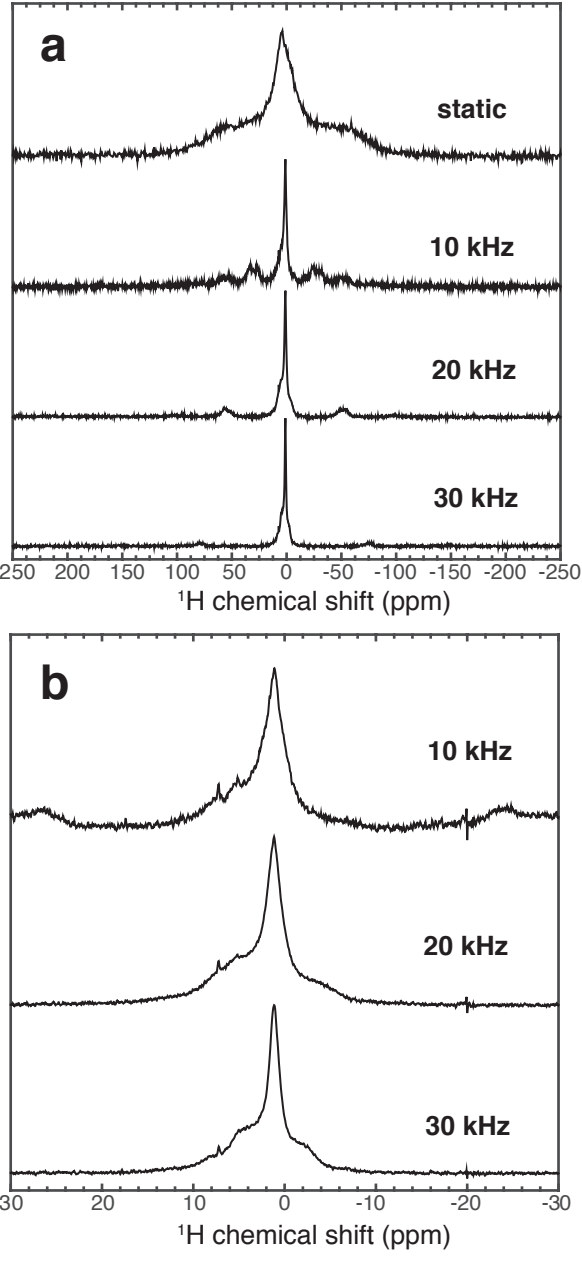
a
static
10 kHz
20 kHz
30 kHz
250 200 150 100 50 0 -50 -100 -150 -200 -250
¹H chemical shift (ppm)
b
10 kHz
20 kHz
30 kHz
30 20 10 0 -10 -20 -30
¹H chemical shift (ppm)

Fig. 2

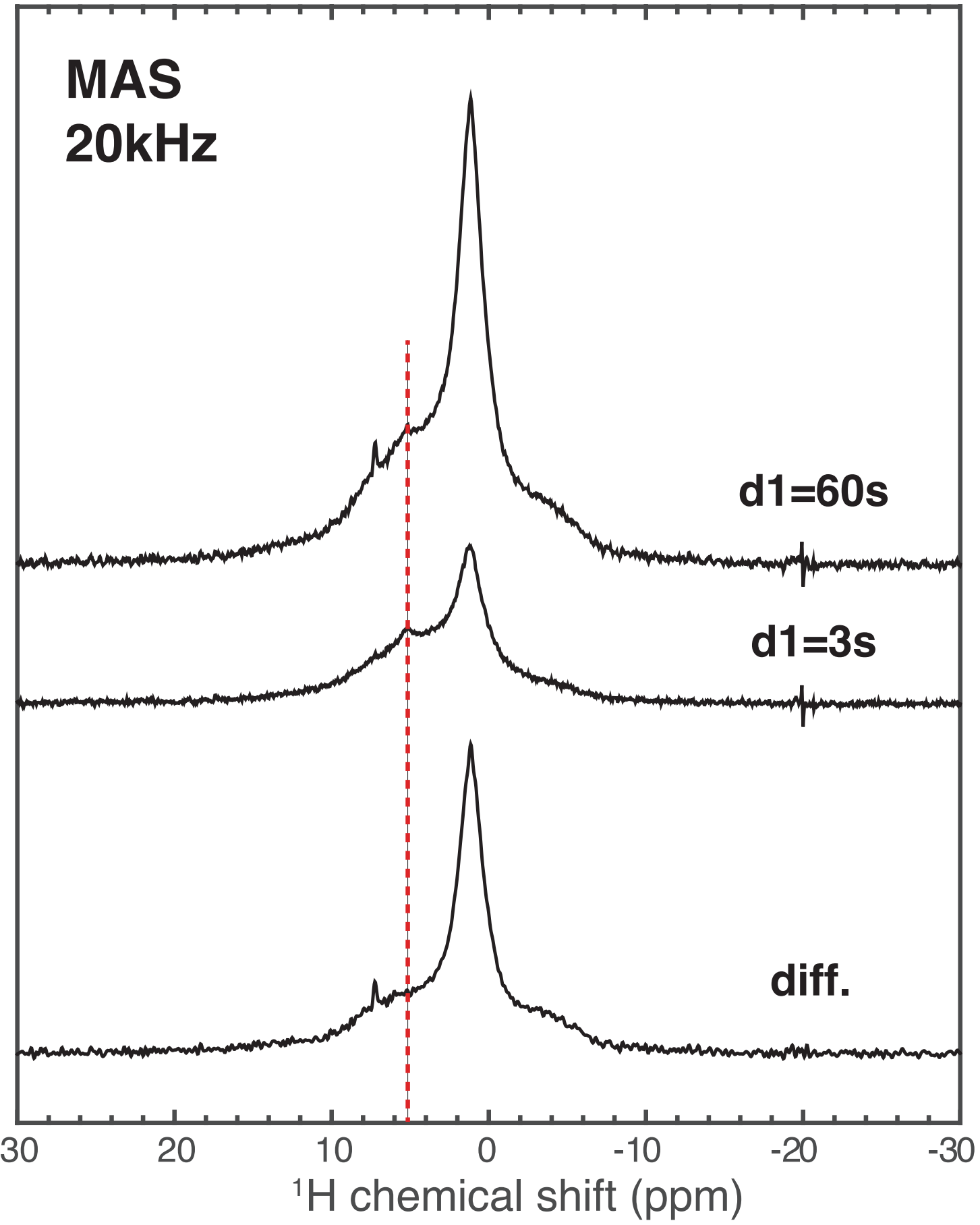
MAS
20kHz
d1=60s
d1=3s
diff.
30
20
10
0
-10
-20
-30
¹H chemical shift (ppm)

Fig. 3

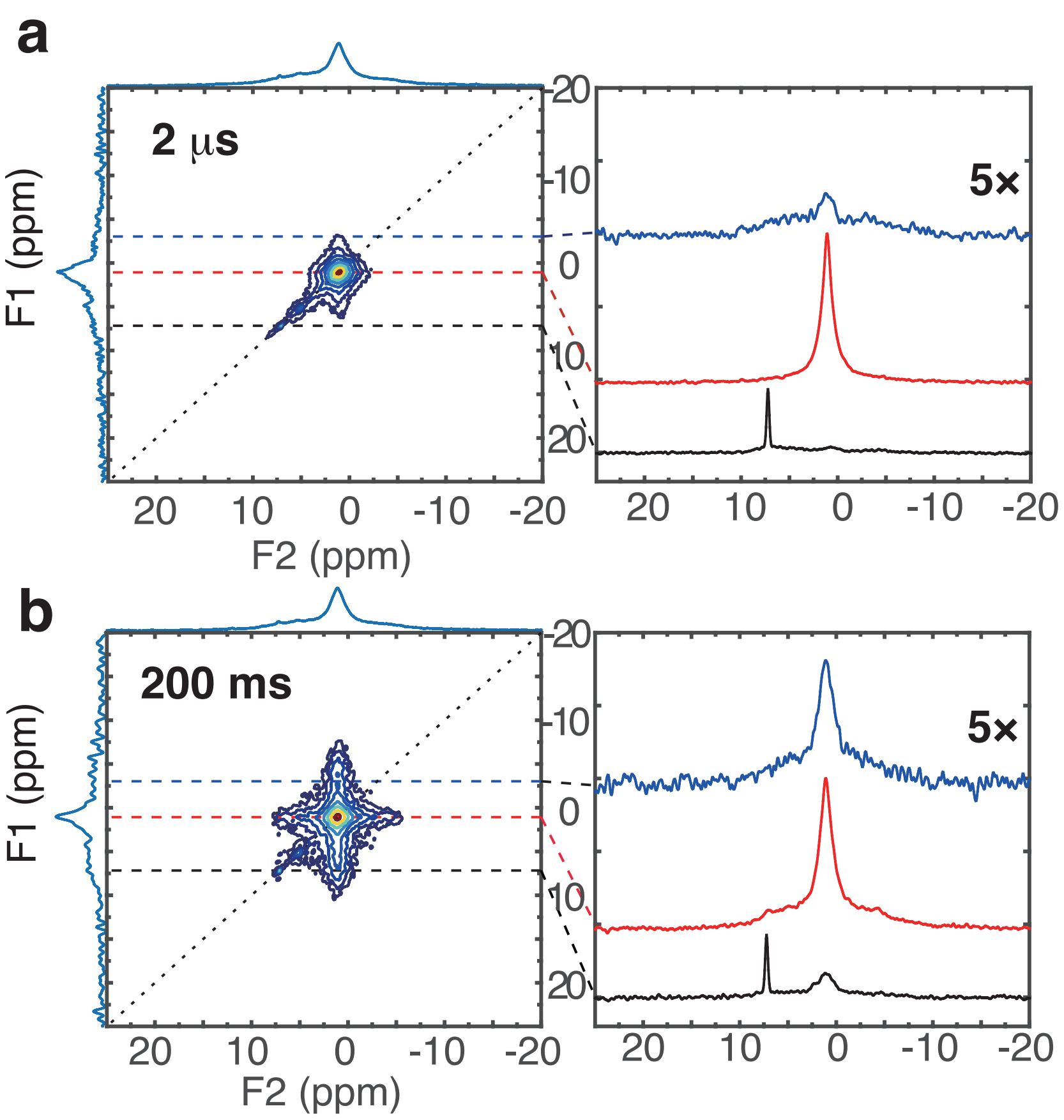

Fig. 4

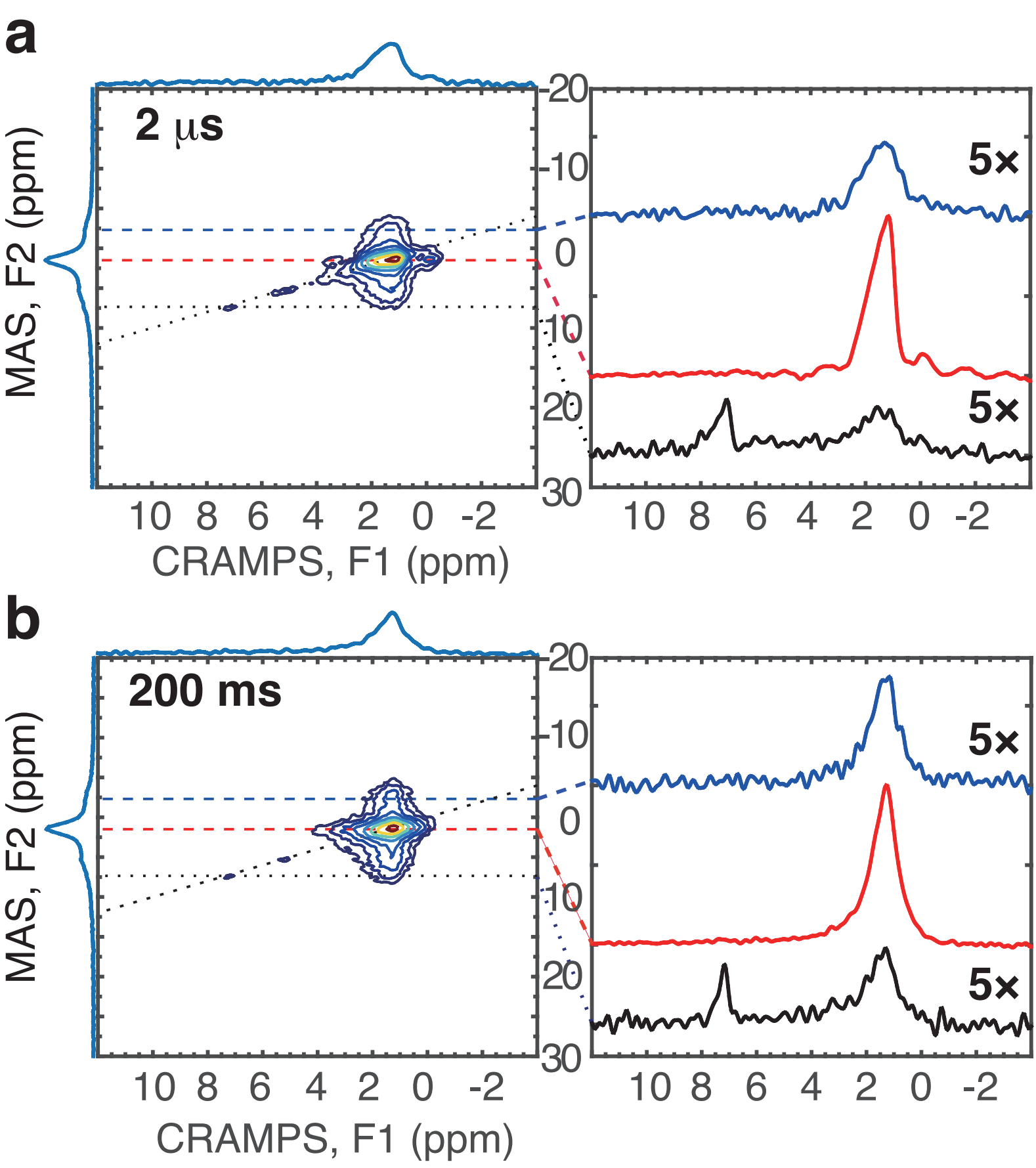
a
2 μs
5×
5×
MAS, F2 (ppm)
CRAMPS, F1 (ppm)
b
200 ms
5×
5×
MAS, F2 (ppm)
CRAMPS, F1 (ppm)

Fig. 5

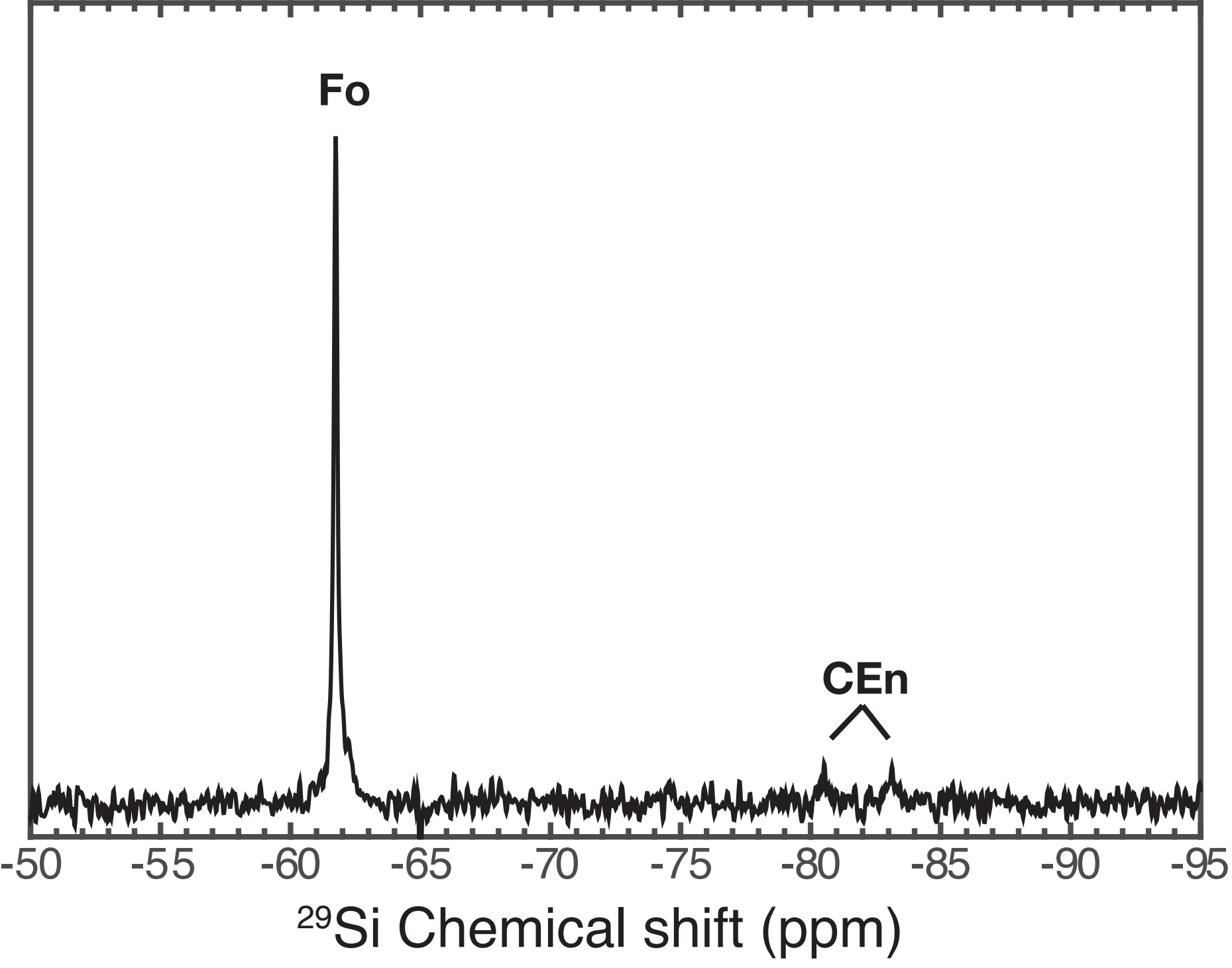

Fig. 6

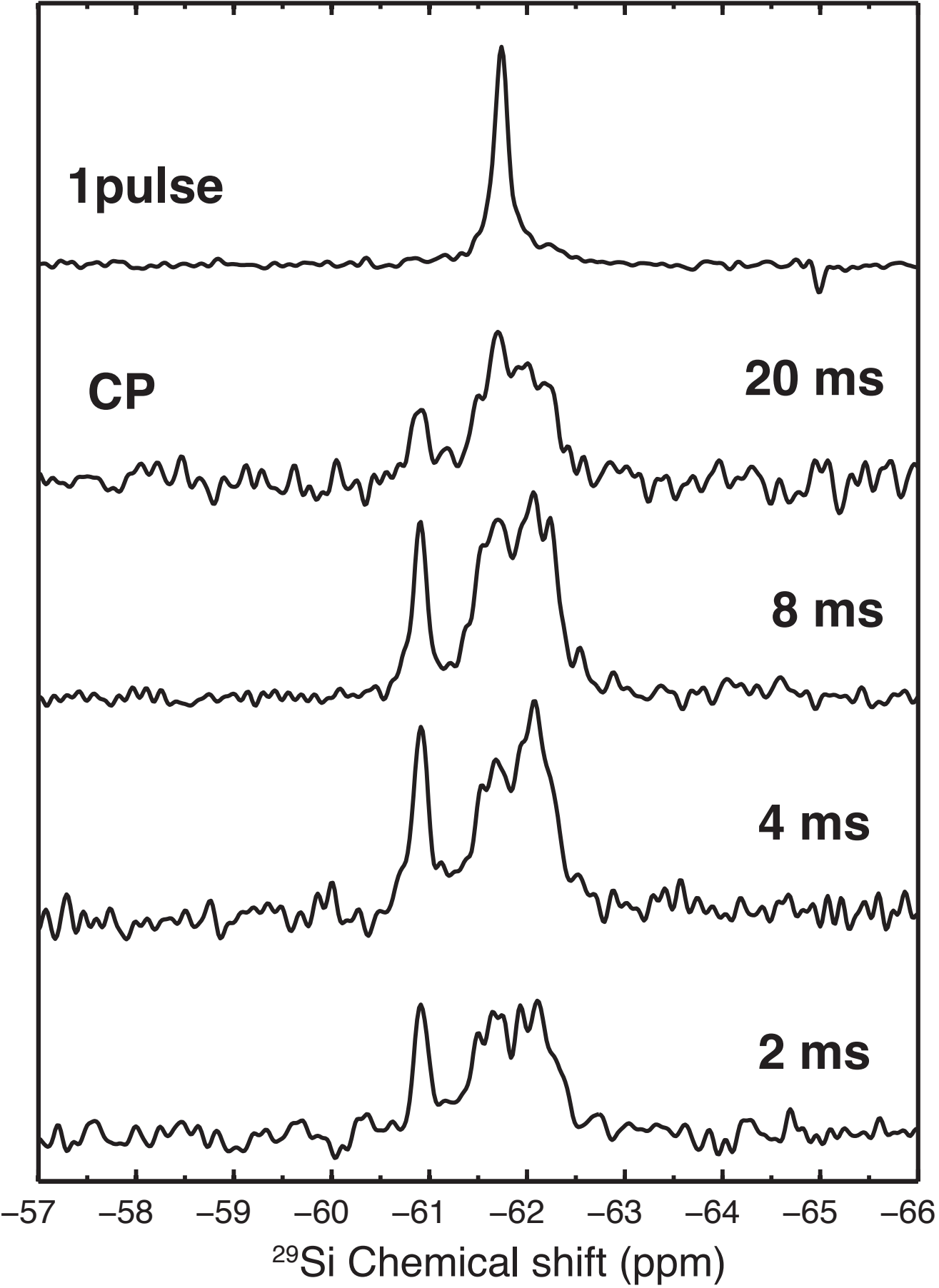
1pulse
CP
20 ms
8 ms
4 ms
2 ms
–57
–58
–59
–60
–61
–62
–63
–64
–65
–66
29Si Chemical shift (ppm)

Fig. 7

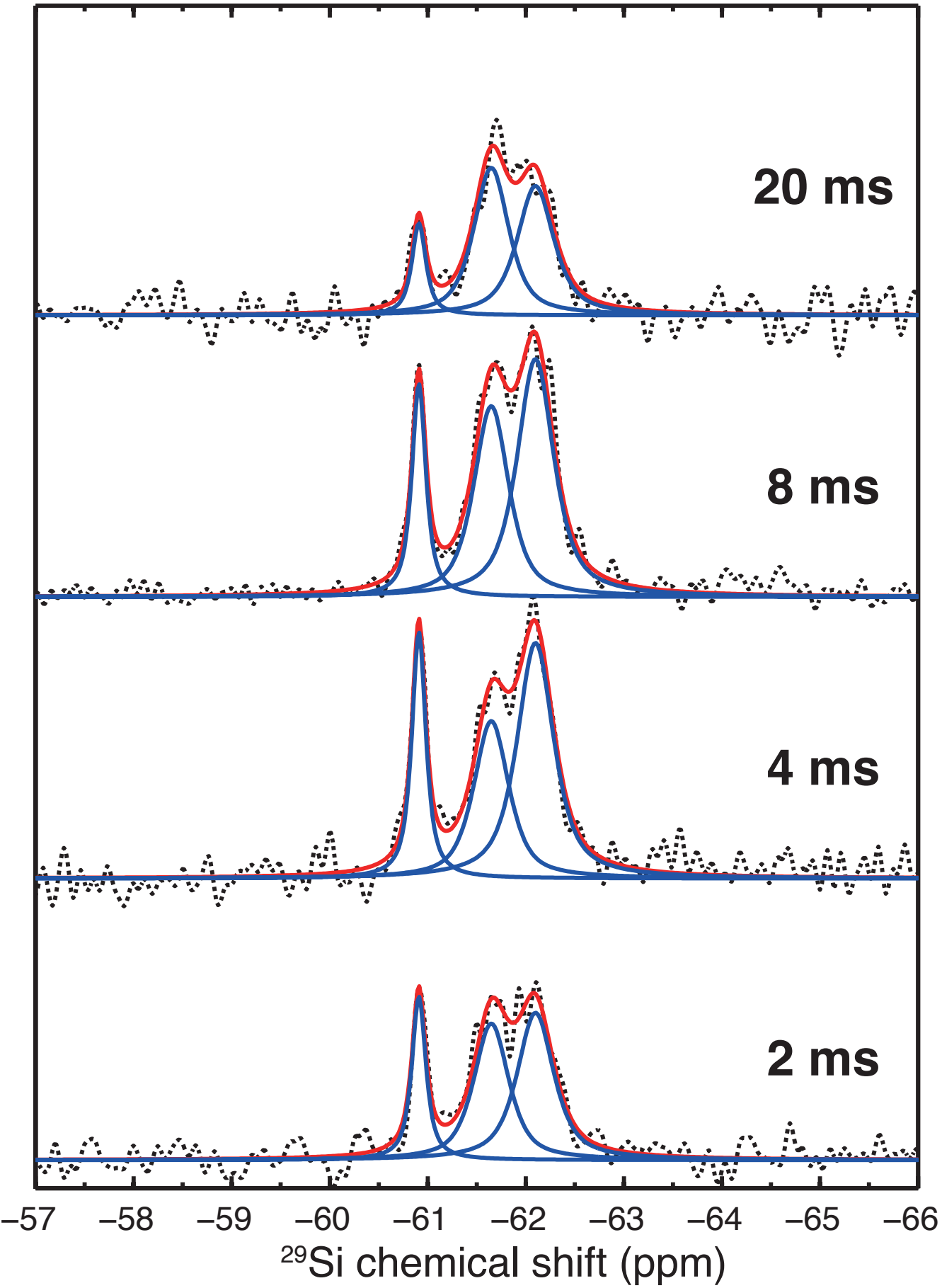
20 ms
8 ms
4 ms
2 ms
−57
−58
−59
−60
−61
−62
−63
−64
−65
−66
29Si chemical shift (ppm)

Fig.8

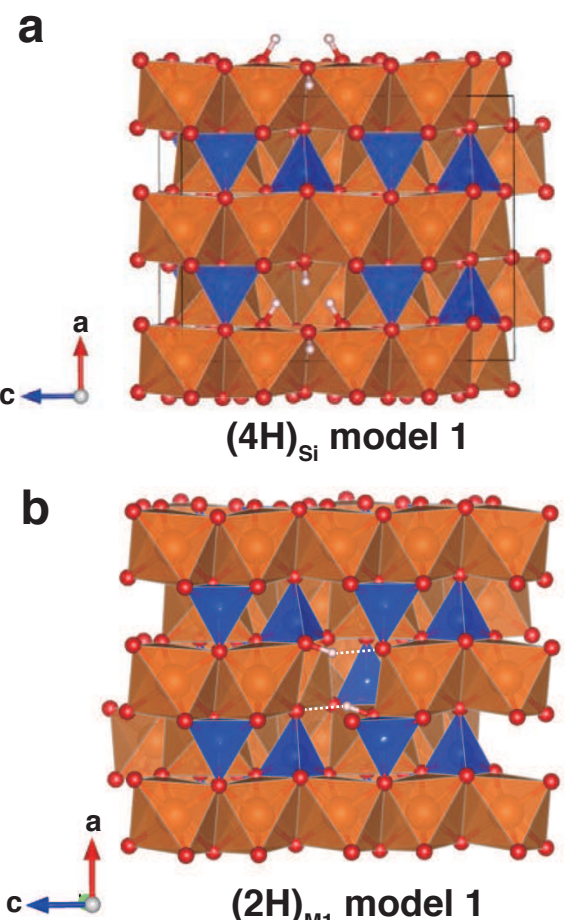

Fig. 9

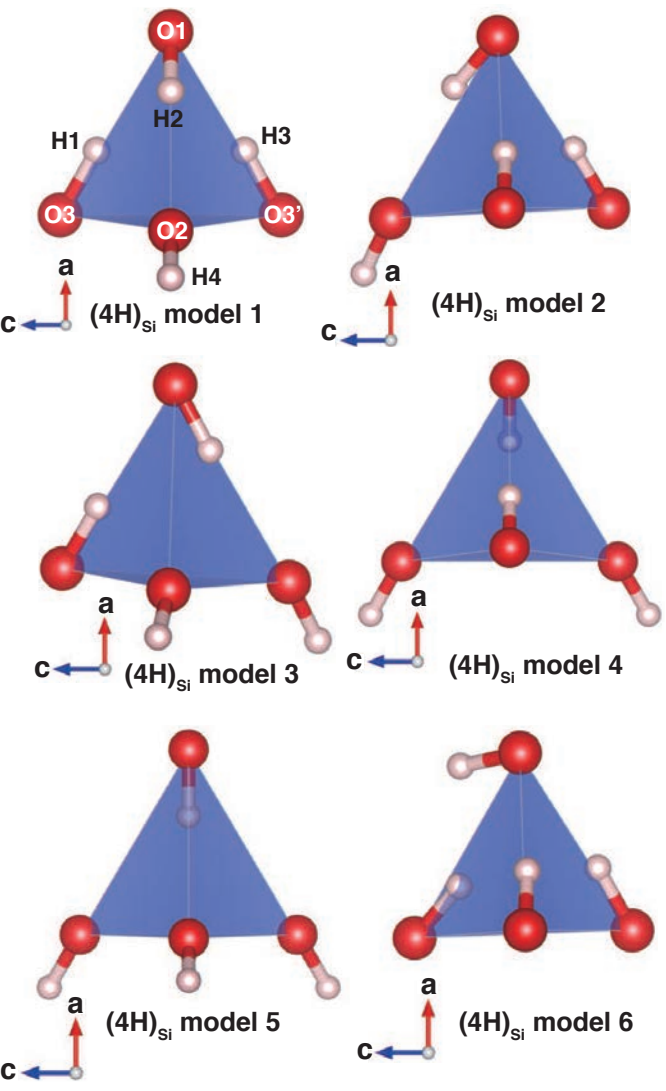
O1
H2
H1
H3
O3
O3'
O2
H4
a
c
(4H)Si model 1
a
c
(4H)Si model 2
a
c
(4H)Si model 3
a
c
(4H)Si model 4
a
c
(4H)Si model 5
a
c
(4H)Si model 6

Fig. 10

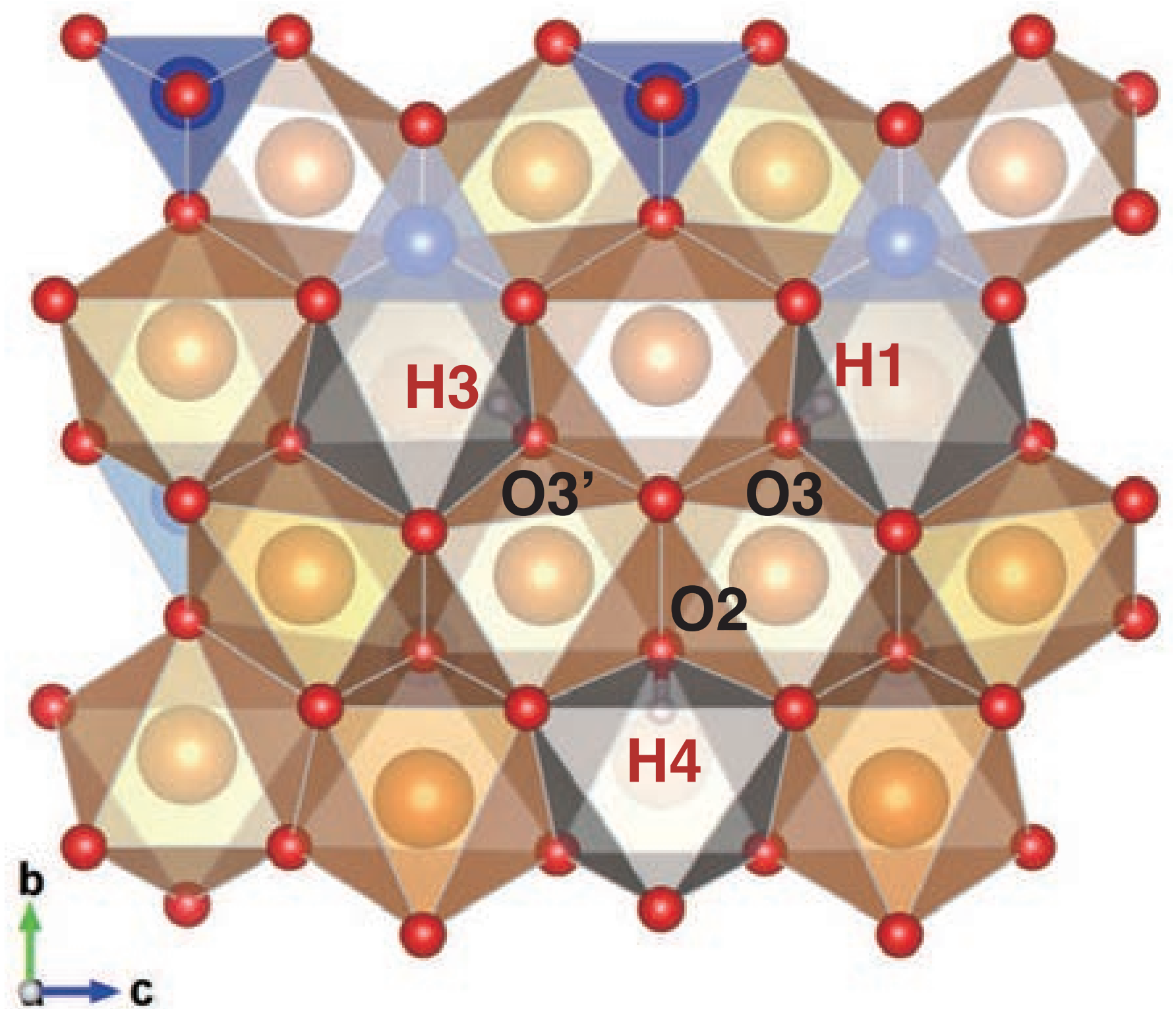

Fig. 11

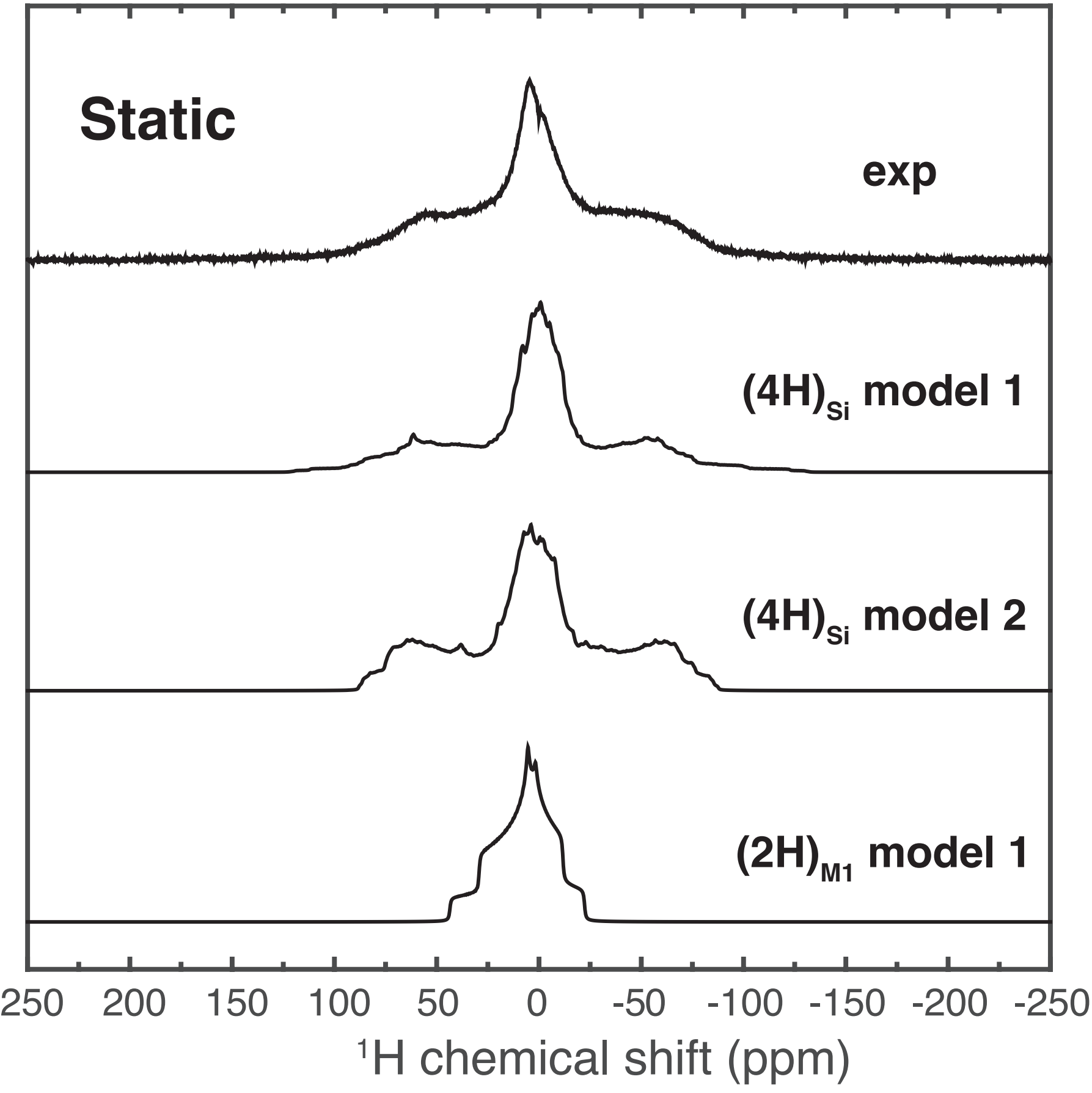
Static
exp
(4H)Si model 1
(4H)Si model 2
(2H)M1 model 1
250 200 150 100 50 0 -50 -100 -150 -200 -250
1H chemical shift (ppm)

Fig. 12

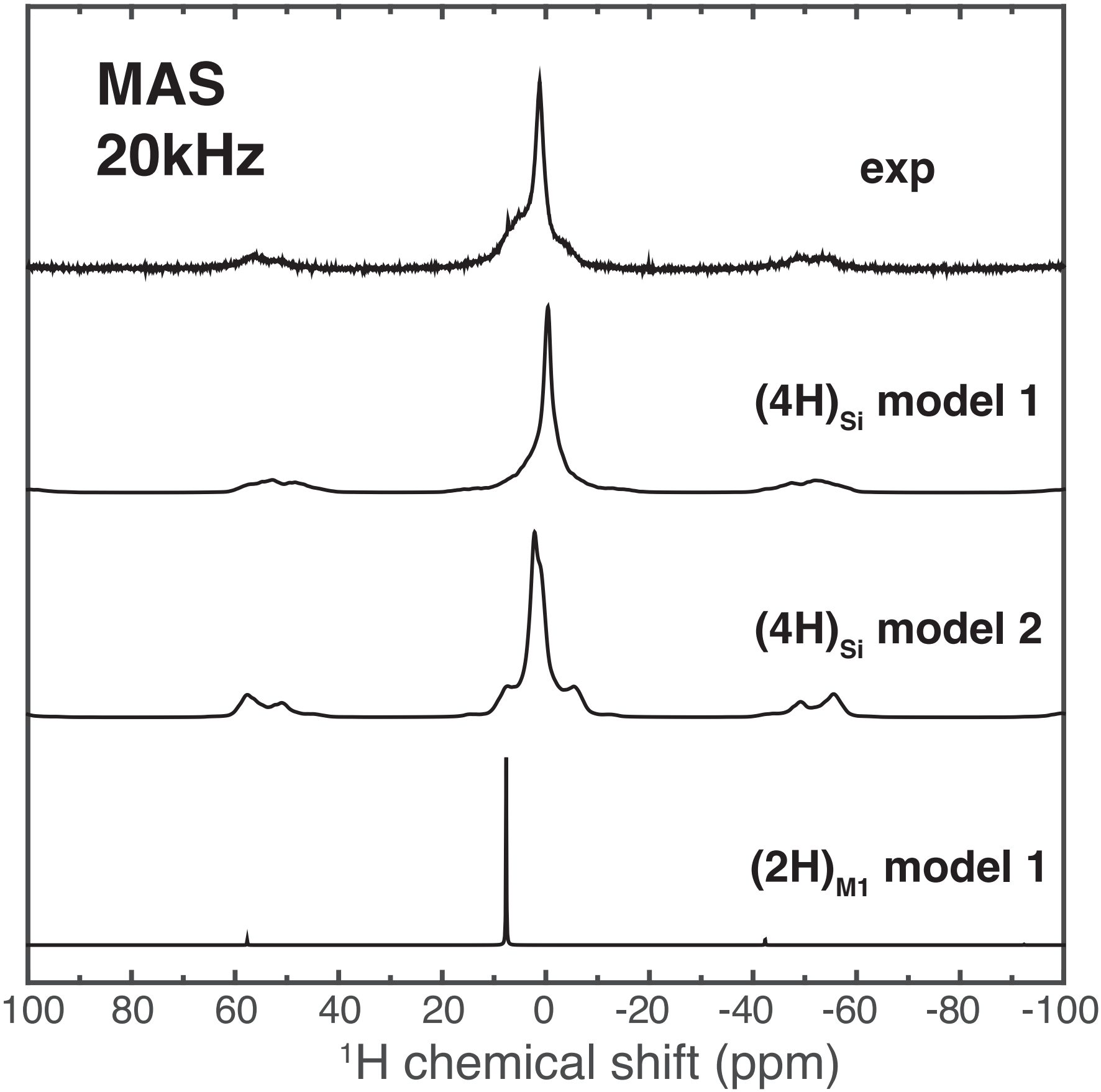
MAS
20kHz
exp
(4H)Si model 1
(4H)Si model 2
(2H)M1 model 1
100
80
60
40
20
0
-20
-40
-60
-80
-100
1H chemical shift (ppm)

Fig. 13